

**Comparisons of Instantaneous TRMM Ground Validation and  
Satellite Rain Rate Estimates at Different Spatial Scales**

David B. Wolff<sup>1,2</sup> and Brad L. Fisher<sup>1,2</sup>

*<sup>1</sup>Science Systems & Applications, Inc, Lanham, Maryland*

*<sup>2</sup>NASA Goddard Space Flight Center, Greenbelt, Maryland*

---

*Corresponding Author's Address:*

David B. Wolff

NASA/GSFC, Code 613.1, Greenbelt, MD 20771

wolff@radar.gsfc.nasa.gov

## Comparisons of Instantaneous TRMM Ground Validation and Satellite Rain Rate Estimates at Different Spatial Scales

David B. Wolff<sup>1,2</sup> and Brad L. Fisher<sup>1,2</sup>

<sup>1</sup>*Science Systems & Applications, Inc, Lanham, Maryland*

<sup>2</sup>*NASA Goddard Space Flight Center, Greenbelt, Maryland*

### Popular Summary

NASA's Tropical Rainfall Measuring Mission (TRMM) was launched in November 1997. This mission was designed to study the global hydrological cycle and to better understand the role of clouds and precipitation in climate change. TRMM collects rainfall information using two different remote sensors on board the satellite – the TRMM microwave imager (TMI) and the Precipitation Radar (PR) – that measure surface rain rates in two distinctly different ways. Three instantaneous and monthly rainfall estimates are derived from these two data sources, using three different rain algorithms, one for the TMI, one from the PR and one that combines data (COM) from both the TMI and the PR. These three rain estimates are not generally in perfect agreement. It is therefore important to understand how they differ and why, and to determine for various climatic regimes, which algorithm performs better, and under what circumstances. In order to make such comparisons it is also important to link these space-borne measurements of rainfall with measurements of rainfall collected at the earth's surface. The primary purpose of this study was to inter-compare the three “instantaneous” satellite products for several different climatic regions using ground-based rain estimates determined from surface weather radars as an empirical reference. The ground estimates for this study used data from three Ground Validation (GV) sites established prior to the launch of TRMM: Melbourne, Florida; Houston, Texas; and Kwajalein Atoll, in the central Pacific Ocean.

The main study was divided into two parts and included all available satellite and GV data from 1999 to 2004. In the first part, instantaneous rain rates from the four rain products were averaged and matched in time and space within a  $0.5^\circ \times 0.5^\circ$  grid, while in the second part, the rain rates were matched at the base resolution of the TMI “footprint” ( $\sim 150 \text{ km}^2$ ) which is quite large relative to base resolution of the PR, COM and GV. For the second part of the study, matching PR, COM, and GV rain rates were averaged inside of the TMI footprint (note there about eight PR and thirty-eight GV pixels fit inside of a single TMI footprint). Both analyses showed good agreement, with the four estimates generally found within 10-15% of each other, but there were some important exceptions, most notably during heavy rain events, when rain rates exceeded  $20 \text{ mm hr}^{-1}$ . This result suggested that one or more of the rain algorithms was either misinterpreting the rain information or the actual observation was providing incorrect information to the algorithm. A preferred mode of precipitation was also observed for TMI at rain rates near  $2 \text{ mm hr}^{-1}$  over the ocean, which was not evident in any of the other estimates. At high rain rates, the COM appeared to perform the best in direct comparisons with GV. The results showed that significant improvements in TRMM satellite rain estimates have been made since the launch of the satellite, but that more work needs to be done to better understand and correct differences between the various algorithms.

## Abstract

This study provides a comprehensive inter-comparison of instantaneous rain estimates from the two rain sensors aboard the TRMM satellite with ground data from three designated Ground Validation Sites: Kwajalein Atoll, Melbourne, Florida and Houston, Texas. The satellite rain retrievals utilize rain observations collected by the TRMM microwave imager (TMI) and the Precipitation Radar (PR) aboard the TRMM satellite. Three standard instantaneous rain products are generated from the rain information retrieved from the satellite using the TMI, PR and Combined (COM) rain algorithms. The validation data set used in this study was obtained from instantaneous rain rates inferred from ground radars at each GV site. The first comparison used  $0.5^\circ \times 0.5^\circ$  gridded data obtained from the TRMM 3G68 product, and similarly gridded GV data obtained from ground-based radars. The comparisons were made at the same spatial and temporal scales in order to eliminate sampling biases in our comparisons. An additional comparison was made by averaging rain rates for the PR, COM and GV estimates within each TMI footprint ( $\sim 150 \text{ km}^2$ ). For this analysis, unconditional mean rain rates from PR, COM and GV estimates were calculated within each TMI footprint that was observed within 100 km from the respective GV site (and also observed by the PR). This analysis used all the available matching data from the period 1999-2004, representing a sample size of over 50,000 footprints for each site. In the first analysis our results showed that all of the respective rain rate estimates agree well, with some exceptions. The more salient differences were associated with heavy rain events in which one or more of the algorithms failed to properly retrieve these extreme events. Also, it appears that there is a preferred mode of precipitation for TMI rain rates at or near  $2 \text{ mm hr}^{-1}$  over the ocean.

This mode was noted over ocean areas of Melbourne, Florida and Kwajalein, Republic of the Marshall Islands, and is shown to exist in TRMM tropical-global ocean areas as well. Further research by algorithm developers is needed to explain or justify the seemingly errant observed probability distributions.

## 1. Introduction

The TRMM GV Program was established early in the planning of the satellite mission. The long-term goal of the GV Program was to determine the accuracy of the satellite rainfall measurements and to identify systematic biases stemming from application of the rainfall algorithms. TRMM GV was structured around two validation strategies: 1) determination of the quantitative accuracy of the integrated monthly rainfall products at GV regional sites over large areas of about 500 km<sup>2</sup> using integrated ground measurements and 2) inter-comparison of the instantaneous satellite and GV rain rate statistics at spatio-temporal scales optimized to the various resolutions of the satellite and GV sensors (Simpson et al., 1988, Thiele, 1988). This current study will address both parts of the validation problem, but will primarily be concerned with validating the instantaneous satellite rain products.

Originally, the primary goal of the TRMM GV program was to determine the accuracy of the TMI, PR and COM rain products on monthly scales over the GV sites. In the pre-mission phase of TRMM, instantaneous validation was still considered problematic because of known differences in the spatial characteristics of the satellite and GV observations. This factor combined with the statistical noise in the data normally encountered at instantaneous time scales made the problem fairly intractable. However, considered at monthly time scales, determining the regional accuracy of the satellite rain estimates based on inter-comparisons with ground-based rain estimates also introduces some intrinsic sources of error, most notably the temporal sampling error of the satellite.

On monthly scales, temporal sampling errors dominate the integrated satellite estimates, and useful comparisons to GV estimates are methodologically difficult to perform. The existence of a large sampling error component complicates the validation of the estimates by entangling the sampling and retrieval errors (Bell T. L., and P. K. Kundu 2000, Bell et al. 2001, Fisher 2007). Various studies have shown have shown that the sampling errors explain at least 8 to 12% of the variance between monthly satellite and GV rain estimates (Laughlin 1981, Shin and North 1988, Bell et al. 1990, Oki and Sumi 1994 and Fisher 2004, 2007).

On the other hand, instantaneous comparisons between coincident measurements are difficult to achieve unless a sufficient number of overpasses are collected and compared. This study uses six years (1999-2004) of satellite overpasses of the GV for comparison with coincident TRMM rain intensity estimates. The data is pixel-matched in both time and space and statistics are provided comparing GV rain intensities (derived via ground-based radars and rain gauges) to the three principal estimates from the TRMM satellite (PR, TMI and COM algorithms). This matching is performed on both a gridded product (3G68,  $0.5^\circ \times 0.5^\circ$ ) and on the TMI footprint scale ( $\sim 150 \text{ km}^2$ ). By performing these comparisons on an instantaneous scale, we are able to remove a large source of uncertainty in the satellite sampling bias.

## **2. Data Sources**

a. TRMM GV

The TRMM GV program's main operational task is to provide quality-controlled rainfall products for four primary sites: Darwin, Australia (DARW); Houston, Texas (HSTN); Kwajalein, Republic of the Marshall Islands (KWAJ); and, Melbourne, Florida (MELB). GV operational rain products provide an empirical surface reference that can be directly compared with similar rain products generated for the two rain sensors aboard the TRMM satellite. The GV rain products provide quasi-continuous long-term coverage at a higher spatio-temporal resolution than can be observed with the satellite, and subsequently provide an empirical means of directly validating the satellite rain estimates, along with other structural and dynamical features associated with propagating rain systems. The TRMM GV program is documented in Wolff et al. (2005), including site and product descriptions, as well as algorithms and data processing techniques. For this study, we used the TRMM 2A-53 instantaneous rain maps that are distributed to the scientific community through the Goddard Distributive Active Archive Center (DAAC). This standard GV product is provided at a resolution of 2 km x 2 km and covers a continuous region extending 150 km from the given GV radar. Each rain map thus consists of a 151 x 151 pixel grid with the GV radar located at the center pixel.

Geographical maps of the gauge and radar networks at DARW, HSTN, KWAJ, and MELB are provided in Fig. 1. Passive microwave rain retrievals are most accurate over the oceans because the homogeneous surface background emissions can be more clearly distinguished from atmospheric emissions associated with clouds and precipitation. The

maps in Fig. 1 maps illustrate one of the key operational dilemmas of TRMM GV: namely, that principally ocean sites, such as KWAJ, that provide the most physically robust comparisons for passive microwave (PM) retrievals instruments on TRMM, provide only limited real estate for deployment of gauges that can be used for calibration and validation of the GV radar rainfall estimates. GV sites with substantial gauge coverage, on the other hand, such as DARW, HSTN and MELB, lack extensive ocean coverage and contain significant coastal areas over which it is inherently difficult, if not impossible, for PM algorithms to robustly estimate rain intensities (as over land the TMI rain estimates are inferred using only the high frequency scattering channels). Although it is well known that there are problems with current PM physical algorithms in coastal areas, we will show that the full-GV-area probability distributions of rain rates are dominantly affected by coastal algorithm uncertainties, and comparison to or validation of TRMM estimates without removing coastal estimates are doomed to failure, or at the very least, misinterpretation.

Figure 2 provides another depiction of the GV sites, illustrating the land/coast/ocean  $1/6^{\text{th}}$  degree mask used by the Version 6 TMI algorithm to delineate geographical type (shaded regions): dark gray is “ocean”, medium gray denotes “coast” (both coastal land and coastal water), and light gray denotes “land”. Also shown are the more subjectively classified geographical types within each of the  $0.5^{\circ}$  grid locations of the TRMM 3G68 product, employed in this study. In these figures, “L” is for land, “C” for coast and “O” for ocean. Additionally, a GV coverage notation is provided (“F” for full coverage, and “P” for partial). The purpose of the coverage flag is to identify pixels that are both fully



observed by the GV radar (i.e. ranges between 15 and 150 km), and that contained a super-majority of one geographical type (i.e. mostly ocean, coast or land, subjectively set at about 60%). For this study only “F” pixels will be considered.

*b. TRMM Satellite: TMI and PR rain sensors*

The TRMM satellite was launched into a sun asynchronous, low-earth orbit on 27 November 1997. The satellite carries a dual-complement of passive and active rain sensors that collect rain information using different remote sensing techniques. TRMM provides data coverage over a continuous annular region of the earth’s surface between 37° S and 37° N. In August 2001, the satellite underwent a boost from an average altitude of 350 km to 402 km. This orbital adjustment was made in order to conserve fuel and extend the life of the mission. Global analysis of instantaneous TMI and PR rain rates indicate that the boost only had a marginal affect on the TMI rain rates, but on average, PR rain rates appear to have been lowered. Systematic changes in the PR rain rates due to boost are still being investigated (J. Kwiatkowski, NASA GSFC 2006 personal communication).

The TRMM Microwave Imager (TMI) passively collects rain information using nine channels at five microwave frequencies: 10.7, 19.4, 21.3, 37.0 and 85.5 GHz. The 21.3 GHz is the only channel that is not dually polarized (only the vertical channel is available at 21.3 GHz). Over land, the TMI rain algorithms only use rain information from the two 85.5 GHz “scattering” channels. The lower frequency channels more

directly probe the precipitable water in the lower regions of the cloud, but over land these channels become contaminated by variations in the microwave emissions from the earth's surface (i.e., non-homogeneous background). Spencer (1989), Conner and Petty (1998) and others have shown that the high frequency scattering channels are correlated with surface rain rates and so can be used as an estimator of rain rate, but since the rain information is communicated by ice-scattering processes occurring above the freezing layer, the relationship between brightness temperature and rain rate is more uncertain and is sensitive to the specific characteristics of the observed rain system. Instantaneous TMI rain rates are generated using the Goddard Profiling Algorithm (GPROF) (Kummerow et al (2001). The algorithm has continued to evolve and significant improvements to the algorithm are described in Kummerow et al (2001) and Olson et al. (2006).

The Precipitation Radar (PR) is the first space-borne radar used in the collection of rain observations. The PR operates at a frequency of 13.8 GHz and has a minimum sensitivity of about 17 dBZ ( $\sim 0.25 \text{ mm hr}^{-1}$ ). The PR's horizontal and vertical resolutions near nadir are about 4.3 km and 250 m, respectively. Its superior vertical and horizontal resolution allows the PR to observe smaller scale precipitation features that cannot be unambiguously resolved by the TMI (Kummerow et al. 1998). However, at 13.8 GHz (2.17 cm wavelength), the PR is strongly attenuated by the intervening rain. The PR rain algorithm subsequently applies a path attenuation correction to the measured reflectivity using the surface reference technique (SRT), resulting in an effective reflectivity factor that is then used in the subsequent estimation of surface and near-surface rain rates (Iguchi et al. 2000; Meneghini et al. 2000). The SRT naturally constrains the PR field of

view (FOV) to a narrow cross-track swath of 250 km (i.e., cross-track scanning angles within  $17^\circ$  of nadir). The attenuation correction can be a significant source of error in cases of heavy rainfall. The spatial sampling of the PR and TMI differ due to differences in areal coverage of each sensor within the orbital track of the satellite, which leads to an expected sampling error for the PR that is about 1.3 times greater than the TMI.

*c. TMI rain algorithm with respect to ocean, land, coast classification*

A detailed description of the specifics of the algorithms of the various TRMM estimates is beyond the scope of this paper, but are well described in the references above; however, it is important to note that distinct differences exist between the land, coastal and ocean retrievals for the various estimates. While there are inherent differences in the actual distribution of rainfall over land and ocean, much of the intra-satellite variance between the TRMM estimates over ocean and land is due to the physical assumptions and intrinsic uncertainties of the retrieval algorithms. The over-ocean TMI algorithm is based on physical models, while the land algorithm is generated empirically (Spencer 1989, Wilheit et al. 2003).

Over ocean, the TMI algorithm estimates surface rain rates using all nine channels to estimate surface rain rates by applying Bayesian statistical methods, relating the measured brightness temperatures to rain rate. The algorithm searches a large database of cloud radiation model simulations to find cloud profiles that are consistent with a given set of microwave radiance measurements. The properties of these profiles are then used

to obtain a best estimate of surface rain rate. The technique is applied only over ocean surfaces because any vertical structure information contained in TMI observations over land or coast is compromised by the strong microwave emission from land surfaces; i.e., microwave emission/absorption by liquid precipitation cannot be easily distinguished from variations in land emission (Tau, et al. 1993, Olson et al. 2006).

Over land, the high and variable emissivity background limits the usefulness of the signal from liquid hydrometeors and only rain information from the two 85 GHz channels are used to determine the surface rain rate. The high frequency channels measure a brightness temperature depression associated with a reduction in received radiation by the satellite due to ice-scattering processes aloft. This ice scattering signal is then matched to a rainfall rate using statistically determined empirical relations between ice aloft and rainfall at the base of the cloud (Wilheit et al. 2003). It is noted that Yuter et al. 2005 found little correlation between the observed scattering signal and low-level reflectivity patterns at KWAJ during the KWAJEX experiment.

These problems are further exacerbated over coastal areas, where ambiguity over the water/land contribution to each footprint becomes problematic from a methodological standpoint, because for either land or water, adding the wrong surface into the footprint has the same effect on observed brightness temperature  $T_B$  as rain (i.e. over land, adding surface water to the footprint will reduce  $T_B$ , as does scattering by rain, and adding land to a water footprint will increase the  $T_B$ s similarly to rain over water, resulting in emission (McCollum and Ferraro 2005).

*d. TMI, PR, COM datasets*

For this study, we used two different data sets for comparison. The first, a gridded product known as 3G68 provides area rain averages in  $0.5^\circ \times 0.5^\circ$  boxes for the TMI, PR and COM algorithms. For the second set of comparisons, we utilized the TRMM Level II footprint data obtained from the satellite-coincidence subsets of 2A12 (TMI); 2A25 (PR) and COM (2B31) products. In this portion of the analysis, we calculated all of statistics at the scale of each individual footprint observed by the TMI that was within PR- and GV-viewable range of the respective GV site.

Table 1 provides the percentage of “land”, “coast” and “ocean” areas for different geographical regions. The TRMM area covers the satellite’s complete sampling domain and is defined from  $35^\circ$  N to  $35^\circ$  S latitude, while the Deep Tropics, a sub-set of this region, is defined between  $10^\circ$  N and  $10^\circ$  S latitude. Note that all sites, except KWAJ, contain significant coastal area, which will be shown to be problematic in the TMI estimates, and also appears to affect the other estimates as well. For brevity, we will provide detailed comparisons of our GV estimates over KWAJ and MELB only, given that KWAJ and MELB are representative of ocean-only and coastal/land areas, respectively. However, we do provide tabular results from our analysis at HSTN. We have excluded DARW from this study principally because of its limited data availability, and its extensive coastal coverage ( $\sim 45\%$ ), which limits its comparative usefulness with the TMI estimates (over ocean). We note, however, that the DARW GV site has played a critical role in the development of the TRMM GV program (Atlas et al. 1993, Rosenfeld

et al. 1992, Rosenfeld et al. 1993, Rosenfeld et al. 1994, Rosenfeld et al. 1995a, Rosenfeld et al. 1995b, Short et al. 1993), and its unique meteorological events provide an extensive and important database for studying both monsoon precipitation and deep-tropical convection dynamics.

### **3. Comparisons of 0.5° x 0.5° gridded data**

For this portion of the analysis, estimates from the TRMM gridded 3G68 product were used to compare to GV rain intensities (Stocker et al. 2001). This product provides area-averaged rain rates using the TMI, PR and COM rain algorithms at a gridded resolution of 0.5° x 0.5°. Each 3G68 pixel that lay over the respective GV sites was extracted and compared to GV estimates obtained by averaging the 2 km x 2km 2A53 rain map pixels to the same 0.5° x 0.5° grid. Thus, the comparisons are matched in both time and space, which removes the process of non-contiguous sampling as a source of uncertainty in these comparisons.

To provide a more detailed comparison, the data from MELB and HSTN were further subdivided into land, coast and ocean categories as defined by the TMI geographical mask, as illustrated in Fig. 2. We note that only pixels with a coverage type of “Full” (F) were used, and thus the sub-sets consisted of all pixels designated as either FO (Full Ocean), FC (Full Coast) and FL (Full Land) types. For KWAJ, there are no land or coast pixels, for algorithmic purposes, it is treated as solely oceanic. We note that Version 5 TRMM algorithms considered KWAJ as nearly 40% coast, given the coarse

grid (0.25°) used at that time. The finer resolution Version 6 TMI surface mask of ~0.166° was also manually modified to exclude classification of small islands and atolls as coastal, prior to implementation of the V6 algorithm (Olson et al. 2006). In this analysis, all GV rain maps (2A-53) from 1999-2004 were used for comparison to the TRMM estimates.

*a. Comparison of monthly means of instantaneous rain rates*

Figure 3 provides a six-panel plot showing the mean monthly rain rate over the selected FO pixels at KWAJ for the period 1999-2004. It is important to note that since these satellite and GV rain rate estimate are matched in time and space, temporal sampling error is not a factor. In order to provide a robust sample, the individual instantaneous comparisons are compiled over monthly (Figs. 3-6), as well as yearly and multi-year (ensemble) time periods (Table 3). Comparative differences between the rain estimates can subsequently be more directly related to algorithmic issues related to retrievals; however, the GV monthly mean in this case should not be considered as empirically representative of the true monthly rainfall. There is good agreement between all of the estimates, with some exceptions, most notably August 2000, May-June 2003, and several months of 2004. Refer to Table 3 for specific values of the annual means and the resultant biases. The biases in Table 2 is defined via equation (1):

$$Bias = \frac{(\overline{E} - \overline{G})}{\overline{G}} \quad (1),$$

where,  $\overline{E}$  is the mean rain rate of the estimate (PR, TMI or COM), and  $\overline{G}$  is the mean

rate from GV. We attribute a high fraction of the inferred monthly biases between the TRMM and GV rain estimates to known calibration uncertainty in the KWAJ radar, described by Wolff et al. 2005 and others (Silberstein et al. 2005, Marks et al. 2005). For KWAJ, using GV as an empirical surface reference, ensemble (1999-2004) satellite-inferred rain biases of -13.7% (PR), -7.9% (TMI) and -5.7% (COM) were observed.

Figure 6 provides the mean monthly rain rate for the various estimates at MELB over FO pixels only. In the case of MELB, though the agreement between satellite-inferred and GV rain estimates are generally good, there is substantial disagreement between the different rain estimates in May 1999. TMI mean rain rates are considerably higher than the other estimates, and in November 1999, the COM rates are considerably lower than the other estimates. There are also significant differences in March-April 2003 between TMI and the other estimates, while the COM estimates are significantly larger than the others during the summer of 2003 and 2004. Figures 7 and 8 provide the monthly mean rain rates for MELB over FL and FC pixels.

Specific values for the annual means and the GV-relative biases are provided in Table 2. The ensemble (1999-2004) MELB, GV-relative biases range from -7.0% to +18.4%, -8.1% to  $\pm 13.9\%$ , and -8.2% to +21.3%, for land, coastal, and ocean areas, respectively. For HSTN, GV-relative biases are on the order of -16.8% to +8.8%, -9% to +18.2%, and -20.3% to +0.7% for, land, coastal, and ocean areas, respectively. Given the lack of sufficient data on a month-by-month basis, the GV-relative biases can be quite large if the mean rain rates are small, thus an ensemble of all 1999-2004 data was used



for these comparisons.

*b. Probability distributions of instantaneous rain rates*

Comparison of the probability distributions (PDF) of TRMM and GV estimates at the  $0.5^\circ$  scale is difficult due to the inherent noise given the somewhat limited sample size; however, the cumulative distribution function (CDF) provides better insight into the comparisons. Figure 8 provides PDF and CDF plots for KWAJ. In this figure, the GV, PR, TMI, and COM distributions are denoted by solid, dashed, dash-dotted and large-dashed lines, respectively. Also shown are the upper and lower quartile and median rain rates for the estimates (thin horizontal dotted lines). At KWAJ, the COM rates are consistently lower than the other estimates, with a median of about  $0.55 \text{ mm hr}^{-1}$ , while the TMI estimates are generally higher than the other estimates with a median of about  $0.7 \text{ mm hr}^{-1}$ . The PR and GV distributions agree well with medians of about  $0.6 \text{ mm hr}^{-1}$ .

Figure 8 provides the ensemble PDF and CDF at MELB for ocean (FO), coast (FC) and land (FL) pixels, in the left, middle and right hand panels, respectively. Over ocean, the CDF agree quite well, with median rain rates differing by less than  $1 \text{ mm hr}^{-1}$ . Over coastal pixels, the scatter among the CDFs is more evident, showing better agreement between the PR and TMI estimates, which are both lower than the GV and COM estimates. In general, the GV distributions fall within the bounds of the other distributions. Over land, there is better agreement between the estimates than over coast, but differences in the CDF are larger than over land. Also, over land, the PR rain rates

are less than the other estimates, while the TMI and GV rates are quite similar.

In summary, our  $0.5^\circ$  gridded comparisons the data show that there is good agreement between the various estimates, and that there are no systematic biases shown between one estimate versus the other. The discrepancies that do occur, are associated with specific (usually heavy) precipitation events; however, overall the TRMM estimates, and the GV estimates to which they are compared, are quite robust and provide a unique dataset for future study of precipitation physics and statistical analyses.

#### **4. Validation at the TMI Footprint Scale**

##### *a. Description of analysis*

Validating the integrated monthly rain estimates from TRMM can provide quantitative error boundaries for regional rainfall estimates used in climate scale applications, but it is not the best GV strategy for physically probing the systematic errors in the satellite rain algorithms, since the rain information in the integrated products is averaged over spatio-temporal scales that are large relative to the resolution of the instantaneous Level II satellite footprint. Moreover, the temporal sampling error of the satellite is a first-order component of the absolute uncertainty in the monthly satellite estimates, which can account for up to 25% of the variance between satellite and ground estimates on monthly scales (Laughlin 1981, Oki et al. 1994, Fisher 2004, Fisher 2007).

The temporal sampling error of the satellite, on the other hand, is effectively eliminated when analyzing instantaneous rain rate estimates at the footprint scale. It is also important to probe the measurements at the footprint scale, because even given coincident, instantaneous observations on larger scales (e.g., TRMM 3G68), small-scale discrepancies due to inter-algorithmic differences in the Level II rain products can be “smoothed out” in the averaging process, limiting the usefulness of such comparisons. Since the spatial autocorrelation function decreases as the spatial averaging scale is reduced down to the footprint scale (i.e., lower signal to noise ratio), many TRMM overpasses are required of a particular region so that the statistical sample can be considered representative of the actual rain rate distribution for that region.

Level II TMI, PR, and COM instantaneous rain rates were matched at the scale of the TMI footprint ( $\sim 154 \text{ km}^2$ ) are statistically compared to Level 2A53 GV radar rain rates at Kwajalein and Melbourne, two sites exhibiting quite different rain climatologies. The data set consisted of six years of overpasses (1999-2004). Table 3 shows that greater than 50,000 pixels were available for each GV site, providing a sufficiently large sample for statistical analysis. The TMI footprint in the Level II rain products is about  $154 \text{ km}^2$ ; however, TMI rain rates are determined from passive microwave radiances collected at five different frequencies, which are elliptically shaped and span a broad range of geophysical scales (Kummerow et al. 1998, Kummerow et. al. 2006). The Level II TMI footprint cannot therefore be thought of as representing a fundamental physical scale, but rather results from an empirical optimization of the rain information covering several

different geophysical scales (Olson et al. 2006). For example, the effective field of view at 10 GHz is  $67 \times 37 \text{ km}^2$ , whereas at 85 GHz the field of view is  $7 \times 5 \text{ km}^2$ .

The satellite domain for Level II instantaneous rain rates (TMI, PR and COM) covers a rectangular area along the TRMM orbital track (2A12, 2A25 and 2B31). The GV radar domain, on the other hand, covers a circular domain that extends 150 km from the radar location. For this analysis, the instantaneous rain rate information was restricted to the geographical intersection of the PR orbital track and the GV radar domain. Figure 11 displays four instantaneous snapshots for the GV, TMI, PR and COM, rain rate estimates for TRMM Orbit #01707 on 10/07/1999 over KWAJ, in the top-left, top-right, bottom-left and bottom-right panels, respectively. These images illustrate the rain rates at the characteristic or native resolution of each of the respective estimates. The red and blue dashed lines illustrate the edges of the orbital track of the PR.

To simplify the procedure, we matched GV, PR and COM to the TMI by considering a 7 km radius around the center of the TMI footprint location. Mean rates were then computed for the GV, PR, and COM at the TMI footprint scale by locating all of the pixels (rainy and non-rainy) found within this circular region (i.e. unconditional averaging). Figure 12 illustrates the same instantaneous snapshots as Fig. 11, but after the GV, PR and COM rain rates were averaged within the respective TMI footprints.

The number of GV, PR and COM pixels associated with each TMI footprint varied from case to case, but tended to average about 8 for the PR and COM (native

resolution of  $\sim 4.3 \text{ km} \times 4.3 \text{ km} \cong 18.5 \text{ km}^2$  resolution) and about 36 for the GV (native resolution of  $2 \text{ km} \times 2 \text{ km} = 4 \text{ km}^2$  resolution). The TMI surface flag was also recorded for each set of matching pixels according to whether the TMI pixel was labeled ocean, land or coast, as described previously. Table 3 gives a summary of the number of overpasses and the number of footprints for each of the four GV locations and lists both the total number of footprints and number of footprints in each terrain category (O, L, C) used in this analysis.

*b. Footprint statistics: means rain rate profiles*

The satellite and GV rain rates were statistically compared at each TMI pixel using GV as an empirical reference for probing the structural distribution of rain rates. The GV rain rates were binned in  $1 \text{ mm hr}^{-1}$  intervals from 0-40  $\text{mm hr}^{-1}$ , along with one additional bin that included all GV rain rates greater than 40  $\text{mm hr}^{-1}$  (due to the relatively small number of samples in the higher bins). The TMI, PR and COM rain rates at each pixel were then matched to the 1 mm bin as determined by the GV rain rate. For example, if the GV rain rate for a given TMI pixel was 5.5  $\text{mm hr}^{-1}$ , the TMI, PR, COM and GV rain rates were all categorically included in the 5 to 6  $\text{mm hr}^{-1}$  bin, irrespective of their rain intensity. The satellite and GV rain rates in each bin were then averaged (as determined from the number of GV rain rates in each bin). Because the rain rates were sorted with respect to the GV rain rate, the mean GV rain rate was by definition confined within the  $1 \text{ mm hr}^{-1}$  rain rate interval for a particular bin and increased monotonically as a function of the rain rate.

After computing satellite and GV means in each binned rain rate category, the rain rate spectrum was sub-divided into two regimes: 1) 0-20 mm hr<sup>-1</sup> and 2) 21-40 mm hr<sup>-1</sup>. Regression parameters were then computed for each of the two regimes (generically referred to here as low and high for the TMI, PR and COM. These parameters are listed in Table 4 and the related scatter diagrams are shown in Figures 11 and 12.

Figure 11 (top left) and 11b (top right) display scatter diagrams for KWAJ, an open ocean climate regime, and MELB, a coastal, sub-tropical climate regime. For the case of KWAJ, all of the points were labeled as ocean, whereas the MELB dataset included a mixture of ocean, land and coast (see Table 1 and Table 3 for TMI surface flag statistics). For Melbourne, the data was also further subdivided according to the TMI surface flag. These scatter diagrams are presented in Fig. 12. See Table 1 for a listing of the number and percentages of ocean, land and coastal pixels for each site.

An examination of the regressions Figs. 11a and 11b for KWAJ and MELB reveals significant differences between the high and low rain rate regimes for the two cases. In the lower rain rate regime, the correlation coefficients between GV and the satellite rain products are all very high ( $R \geq .95$ ). Figure 11, considered together with Table 4, indicates a positive, linear relationship between the satellite and GV rain rates in the low rain rate regime. The slopes show some systematic differences in the mean rain rates statistics, but the agreement between GV and the satellite rain rates are generally very good in the low rain rate regime. The correlations, however, drop off significantly in

the higher rain rate regime for the TMI and PR due to increasing variance and a deviation from the simple linear relationship observed in the lower regime.

The GV-TMI regression shows a distinctive leveling off relative to GV in the high rain rate regime, which is characterized by a sharply decreasing slope parameter, increased variability and a diminishing correspondence with GV. Ha and North (1995) point out that above  $20 \text{ mm hr}^{-1}$  the scattering of microwave radiation becomes important and causes the relationship between rain rate and brightness temperature to become double-valued. For the TMI, mean rain rates also never exceed  $30 \text{ mm hr}^{-1}$ . Compared to GV, the breadth of the TMI rain rate distribution is more narrow and skewed and results from the statistical characteristics of the distributions at the high end (rain rate  $> 20 \text{ mm hr}^{-1}$ ).

We attribute the flattening out of the TMI profile to the saturation of the lower frequency TMI channels and beam filling effects associated with high rainfall gradients. High rainfall gradients pose problems for the TMI rain algorithm due to the non-uniform rain area in the field of view (FOV) of the low frequency TMI channels (Wilheit et al. 1991; Kummerow 1998; Kummerow et al. 2001). Beam filling smear the rain field over a larger area, resulting in a systematic underestimation of the rainfall. Beam filling errors are most significant in cases where large brightness temperature gradients exist in association with smaller scale convection. Small-scale convective systems are quite common across the Florida Peninsula and around Kwajalein (which is located in the ITCZ). TMI rain rates over land in the case of MELB trend higher than for the ocean case, but are still substantially lower than what was observed for GV.

In the latest version of GPROF (version 6), the problem of rain heterogeneity has been treated in such a way that the uncertainty no longer depends on the computation of a convective-stratiform ratio and instead varies as a constant factor (Kummerow et al. 2001). The saturation problem was addressed in the original design of the TMI sensor. Based on prior experience with SSM/I, the water vapor channel was shifted from 22.235 to 21.3 GHz to avoid saturating the signal, in which high brightness temperatures in the 21.3 GHz channel are correlated with high rain rates (Kummerow et al. 1998), but this sensor modification obviously did not eliminate the problem entirely.

The PR rain rate profile displays more consistency than the TMI profile between the low and high rain rate regimes, but like the TMI, it too flattens out in the high rain rate regime. Looking at Figs. 11a and 11b, the higher PR rain rates are also more tightly distributed around the regression line, but do not exceed  $30 \text{ mm hr}^{-1}$  in either of the two profiles, and appear higher for KWAJ than MELB. Regional climatology associated with rudimentary differences in the DSDs may be a significant factor, but in the case of GV, the effective Z-R is determined using the probability matching method, which naturally accounts for differences in DSD without the need for any assumptions about the structure of the distribution (Rosenfeld, 1994). DSD differences can also affect the attenuation correction applied to the raw reflectivity data (Iguchi et al. 2000).

The high rain rates in the case of the TMI are physically constrained for the reasons discussed above. The PR is an active rain sensor and is not limited by these same



constraints that effect passive microwave observations, and so the lower mean rain rates in the PR profile is not necessarily an indication that that higher rain rates do not exist, but rather suggests that there are fewer high rate observations than GV, and that when they do occur they are being matched at lower GV rain rate and subsequently result in a lower average (i.e., a high PR rain rate are being mixed with lower rain rates, which effectively lowers the average). Furthermore, when the PR data is further stratified into ocean, land and coastal areas as seen in Figs. 12a, 12b and 12c for MELB, the PR ocean and land profiles generally flatten out and show less correspondence with GV. PR coast shows the best agreement at the high rain rates. Note that the PR algorithm does not depend on the TMI surface flag, but does depend on its own determination of stratiform and convective rain areas, which affects the DSD profile used to convert reflectivities to rain rate.

Amitai et al. (2006) have shown that modifications to the V6 algorithm produce different pdfs when compared to GV over Melbourne, Florida, and even though V5 contained regional biases, the pdfs were in better agreement with GV. The most significant V6 algorithmic changes mainly affected the rain type classification and the application of the attenuation correction. Amitai et al. 2006 reported that V6 changes resulted in a reduction of 26% of the convective rainfall and a 13% increase in the amount of stratiform rain. These observed changes would have the effect of shifting the higher rain rates lower relative to V5, which appear consistent with the results observed in this study.

The COM-GV regression generally exhibited less de-correlation at higher rain rates for KWAJ and MELB and rain rates in both the high and low regime tended to increase monotonically with respect to the matching GV rain rates. The COM rain rates are generated using a rain algorithm that utilizes information from both the TMI and PR resulting in the hybrid 2B31 rain product (Haddad et al. 1996). For the KWAJ case shown in Fig. 11a, the COM slope in the high regime increases relative to the low regime. The TMI and PR slopes both exhibited decreases. The COM also observed a greater frequency of rain rates at the high end of the dynamic range, a profile characteristic observed for both KWAJ and MELB. Although COM shows some consistency with the PR in the case of KWAJ, for the case of MELB, it deviates from the PR and the TMI in the high regime, especially in the land and coast stratifications. These results are very encouraging and suggest that significant improvements in rain estimation can be realized using information from both sensors, even when the individual sensors exhibit different rain characteristics relative to the hybrid product.

*c. Footprint statistics: standard errors*

Satellite errors were estimated over a dynamic range between 0 and 35 mm hr<sup>-1</sup> by computing the relative variance,  $\sigma_{err}^2(i)$ , between the satellite and the GV mean rain rate for a given rain rate bin, using the following expression:

$$\sigma_{err}^2(i) = var(s_i - \bar{r}_i) = \sigma_s^2(i) + \sigma_r^2(i) - 2cov(s_i, \bar{r}_i) \quad (2),$$

from which the standard error is then computed by taking the square root of the resulting variance:

$$\sigma_{err}(i) = \sqrt{\text{var}(s_i - \bar{r}_i)} \quad (3)$$

In (2) and (3),  $s_i$  and  $\bar{r}_i$  correspond to the satellite and GV rain rate for the  $i^{\text{th}}$  rain rate bin as determined by GV. Consequently, the main contributions to the error in (3) come from the two terms  $\sigma_s$  and  $2\text{cov}(s_i, \bar{r}_i)$ , since the statistical distribution for  $\bar{r}_i$ , as represented by  $\sigma_r$ , is confined within a 1 mm/hr interval as described 4b.

A 3-bin averaging filter was then applied at each point to reduce some of the inherent noise encountered at 1 mm hr<sup>-1</sup> intervals, especially at the high end. In this case we are interested in the more general features of the profile and less concerned with the point-to-point variability. Figure 11 c-d and Fig. 12 d-f display plots of the results for KWAJ and MELB comparing the standard errors in the satellite rain rates versus the GV mean at each 3 mm hr<sup>-1</sup> interval.

In all the cases considered, standard errors tend to increase monotonically (though this behavior is not strictly true across the full range of rain rates) from near 0 at the low end to as high 15 mm hr<sup>-1</sup> at the high end. Standard errors in the nominal part of the rain rate spectrum tend to be the lowest for the oceanic case, but show sharper increases for rain rates above 25 mm hr<sup>-1</sup>. TMI standard errors over ocean also trended lower than the PR and COM for both KWAJ and MELB, whereas TMI errors trended substantially higher over land and coast for the MELB case. Our results are consistent with results

from Olson et al. (2006). They computed standard errors at the footprint scale (ocean only) based on seven complete TRMM orbits and showed similar monotonically increasing behavior between a range 0 and 18 mm hr<sup>-1</sup> across a dynamic range of estimated rain rates that runs from 0 to 30 mm hr<sup>-1</sup>. The results suggest the possibility some regional dependence at the higher rain rates. The TMI profiles for MELB and KWAJ, for example, are fairly similar in the lower range of rain rates below 20 mm/hr, but diverge above 20 mm/hr, with MELB exhibiting more sharply increasing errors relative to KWAJ. The COM and PR oceanic profiles for MELB also exhibit a pronounced bump in the profile between 25 and 27 mm/hr, with a relative maximum at 26 mm/hr (which has undergone a 3-point smoothing). A similar feature seems to be present for KWAJ as well, though the relative maximum in the COM profile is clearly not as pronounced in the KWAJ case. More analysis will be required to verify these inferred error characteristics.

*d. Probability distributions at the TMI footprint scale.*

Figure 13 provides the PDF and CDF rain rates for each estimate at the footprint level at KWAJ. Also, shown are the resultant mean rain rates (2.01, 1.59, 1.83 and 1.61 for GV, PR, TMI and COM, respectively), as well as the total number of ‘footprints’ that were used for averaging the various estimates. Given the large number of points available for generating these distributions, much can be deemed by analysis of the individual PDFs. Most notably, note that the basic shapes of the GV, PR and COM

estimates are quite similar, with peaks on the low end near  $0.5 \text{ mm hr}^{-1}$ ; however, the TMI distributions is much more peaked with a pronounced mode at about  $2 \text{ mm hr}^{-1}$ .

Overall, the COM and PR CDFs agree the best, and the TMI estimates are considerably higher at all rain rates up to about the 90<sup>th</sup> percentile (just over  $2 \text{ mm hr}^{-1}$ ). Again, as in Section 3, we see that the GV CDF falls within the bounds of the other CDFs. An interesting set of questions arises here as to why the TMI PDF is so dissimilar to the other PDF? Is this due to land affects of the atoll on the TMI estimates (which the algorithm assumes do not exist), or is this an inherent issue with TMI PDFs over ocean? Others have shown some unusual characteristics of TMI oceanic PDFs. In a global study, Yuter et al. 2006 showed that there are preferred regions where TMI PDFs can be described as “physically implausible.”

To determine whether the land areas of the atoll affected the TMI estimates, we subdivided the KWAJ GV domain as illustrated in Fig. 14. In this figure, the shaded regions directly over KWAJ were designated as “coast” with the remainder of the areas (white region within 150 km from the radar) are designated as “ocean”. As mentioned previously, this rather crude mask, which was used in all TMI products prior to Version 6, was at  $0.25^\circ$  resolution. Any  $0.25^\circ$  pixel that contained land mass was assumed to be either coast or land (depending on the amount of land in the given pixel), and using this classification resulted in KWAJ being considered approximately 40% coast (for algorithmic purposes). We note that the products used for this comparison were still Version 6, but the geo-type classification was via Version 5 surface masking. Figure 13

shows the PDF of KWAJ rain rates for the various estimates, for All (as per Figure 12), Ocean (V5-deemed ocean pixels), and coast (V5-deemed coastal pixels) in the left, middle and right hand panels, respectively. While the resultant means are slightly different, the distributions themselves are nearly indistinguishable, which seemingly contradicts the hypothesis that land affects caused the different behavior of the TMI PDF versus the PDF of the other estimates.

To investigate whether or not this is possibly due to an inherent issue in ocean TMI estimates, we used a dataset of distributions of TMI rain rates over  $2.5^\circ$  pixels throughout the tropics compiled by T. Bell (NASA GSFC 2006 *personal communication*). Figure 16 shows an ensemble of monthly PDFs for the period 1999-2004, for ocean, land and coast, in the left-, middle- and right-panels, respectively. The ocean PDFs clearly show a preferred mode of about  $2 \text{ mm hr}^{-1}$ , as seen over KWAJ and MELB, indicating that there is indeed some algorithmic preference for such estimated rain rates. The land PDF shows the difficulty of estimating light rain rates, given the restrictions imposed by the sole use of scattering as a precipitation estimate. We note also that the TMI observed rain rates are significantly higher over land than ocean. This fact is due to both actual differences in precipitation characteristics over land and ocean, and the failure of current TMI to estimate higher rain rates over ocean due to the saturation of the signal and beam-filling issues discussed previously.

## **5. Summary and Conclusions**

A comparison of TRMM satellite and GV rain intensity data has been conducted for the period 1999-2004 at two different scales:  $0.5^\circ \times 0.5^\circ$  (corresponding to the resolution of the TRMM 3G68 product), and at the nominal scale of the TMI footprint ( $\sim 150 \text{ km}^2$ ). It was shown that all of the estimates agree well, but there were some notable differences, especially during heavy rain events. The observed differences were seen to be related to each rain sensor's ability to resolve different precipitation events, differences between the rain information collected by active and passive remote sensing techniques and systematic variations in the physical applications of the rain algorithms.

Some of the discrepancies were shown to be dependent on the geographical terrain over which the various estimates were made. Over land, for example, the TMI algorithm cannot resolve light rain rates (less than approximately  $0.8 \text{ mm hr}^{-1}$ ) because the algorithm only uses the 85 GHz scattering signal and this precipitation tends not to be highly correlated with ice processes aloft. The TMI coastal algorithm was also shown to have problems due to the partitioning of these regions into land and ocean sectors. This poses an intrinsic problem for GV, for as was shown in Table 1, GV sites consist of a much higher fraction of coastal pixels relative to the complete sampling domain of the TRMM satellite. In the case of the PR, on the other hand, attenuation of the high frequency radar signal limits the ability of the PR to resolve areas of deep convection over land and to some extent over ocean. Over ocean, the TMI is better able to resolve the lighter rain rates (about  $0.02 \text{ mm hr}^{-1}$ ), but the precipitation signal in the lower channels becomes saturated at higher rain rates (approximately  $20 \text{ mm hr}^{-1}$ ). Moreover, it was shown that there is a preferred mode in the TMI rain rate distributions at or near 2

mm hr<sup>-1</sup> that was not evidenced by any of the other estimates, thus indicating that more work need to be done to improve the over-ocean estimates by the TMI algorithm.

While analysis of the probability distributions was difficult for the 3G68 comparisons, due to limited sample size, a much more robust number of observations was possible at the TMI footprint scale (approximately 12000 and 9200 samples per year for KWAJ and MELB respectively). The subsequent analysis performed showed that the PDFs of the GV, PR and COM were quite similar to one another. The TMI PDFs compared to other three revealed significant structural differences. One of the key findings of this work is the pronounced effect that coastal areas have on the retrieved distribution of rain rates, especially by the TMI. Although it is well known that there remain problems to resolve with current passive microwave techniques with respect to the estimation of rain intensities over coastal areas, it was shown that the full-GV-area probability distributions of rain rates are ~~dominantly~~ strongly affected by coastal algorithm uncertainties. Consequently, validating TRMM estimates without removing coastal estimates will significantly increase the quantitative uncertainty, and at the very least, lead to a misinterpretation of the results. At the footprint scale, the COM algorithm, interestingly, appeared to significantly out perform both the TMI and the PR at the higher rain rates, based on statistical comparisons with GV. Generally, the observed improvement related to a stronger linear correlation with GV at the higher rain rates, whereas the slope parameters for TMI and PR both tended to exhibit more flattening in this region of the rain rate spectrum, especially in the case TMI due to saturation of the signal. It was seen that increased variability at the higher rain rates (i.e., > 20 mm/hr)



also led to sharp increases in the observed errors considered as a function of rain rate relative to the GV rain rate spectrum. The standard errors observed, though tending to increase monotonically with rain rate, depended on the region (KWAJ or MELB), geographical terrain (land, coast ocean) and climate. Additional work by algorithm developers is needed to further refine the differences in the satellite retrievals.

## **5. Acknowledgements**

The authors would like to thank Dr. Ramesh Kakar (NASA Headquarters), Dr. Robert Adler (TRMM Project Scientist) and Mr. Richard Lawrence (Chief, TRMM Satellite Validation Office) for their support of this effort. We also appreciate the support staff of the TSVO, including David Makofski, Bart Kelley, David Marks, David Silberstein, and Jason Pippitt.

## References

- Amitai, E., X. Lloret, and D., Sempere-Torres, 2006: *Opportunities and challenges for evaluating precipitation estimates during GPM mission*. Meteorologische Zeitschrift, **15**, 551-557.
- Atlas, D., D. Rosenfeld and D. B. Wolff, 1993: On climatological C-band attenuation by rainfall using probability matched reflectivity-rainrate functions. *J. Appl. Meteor.*, **32**, No. 2, 426-430.
- Bell, T., L., A. Abdullah, R. L. Martin and G. North, 1990: Sampling errors for satellite-derived tropical rainfall: Monte Carlo study using a space-time stochastic model. *J. Geophys. Res.*, **95**, 2195-2205.
- Bell T. L., and P. K. Kundu, 2000: Dependence of satellite sampling error on monthly averaged rain rates: comparison of simple models and recent studies. *J. Appl. Meteor.*, **13**, 449-462.
- Bell, T., L., P. K. Kundu, and C. D. Kummerow, 2001: Sampling errors of SSM/I and TRMM rainfall averages: Comparison with error estimates from surface data and a simple model. *J. Appl. Meteor.*, **40**, 938-954.

- Conner M.D., and G. W. Petty, 1998: Validation and intercomparison of SSM/I rain-rate retrieval methods over the continental United States. *J. Appl. Meteor.*, **37**, 679-700.
- Fisher, B. L., 2007: Statistical error decomposition of regional-scale climatological precipitation estimates from the Tropical Rainfall Measuring Mission (TRMM). *J. Appl. Meteor. and Climatol.*, in press.
- Fisher, B. L., 2004: Climatological validation of TRMM TMI and PR monthly rain products over Oklahoma. *J. Appl. Meteor.*, **43**, 519-535.
- Ha E., and G. R. North, 1999: Error Analysis for some ground validation designs for satellite observations of precipitation. *J. Atmos. Oceanic Technol.*, **16**, 1949-1957.
- Haddad, Z. S., E. Im, S. L., Durden, and S. Hensley, 1996: Stochastic Filtering of Rain Profiles Using Radar, Surface-Referenced Radar, or Combined Radar–Radiometer Measurements. *J. App. Meteor.*, **35**, 229-242.
- Iguchi, T., T. Koizu, R. Meneghini, J. Awaka, K. Okamoto, 2000: Rain-profiling algorithm for the TRMM precipitation radar. *J. Appl. Meteor.*, **39**, 2038-2052.
- Kummerow, C. W. Barnes, T. Koizu, J. Shiue, J. Simpson, 1998: The tropical rainfall measuring mission (TRMM) sensor package. *J. Atmos. Oceanic Technol.*, **15**, 809-817.

- Kummerow, C., 1998: Beamfilling errors in passive microwave rainfall retrievals. *J. Appl. Meteor.*, **37**, 356-369.
- Kummerow, C., and Coauthors, 2001: The evolution of the Goddard profiling algorithm (GPROF) for rainfall estimation from passive microwave sensors. *J. Appl. Meteor.*, **40**, 1801-1820.
- Kummerow, C. W. Berg, J. Thomas-Stahle, and H. Masunaga, 2006: Quantifying global uncertainties in a simple microwave rainfall algorithm. *J. Atmos. Oceanic Technol.*, **23**, 23-36.
- Laughlin, C. R., 1981: On the effect of temporal sampling on the observation of mean rainfall. *Precipitation Measurements from Space*, D. Atlas and O. Thiele, Eds., NASA Publication, D59-D66.
- Marks, D.A., D.B. Wolff, D.S. Silberstein, J.L. Pippitt, and J. Wang, 2005: Improving radar rainfall estimates at Kwajalein Atoll, RMI through relative calibration adjustment, *Preprints, 32<sup>nd</sup> Conference on Radar Meteorology, 3R.1 AMS* Albuquerque, NM, October 24-29, 2005.
- McCollum, J. R., R. R. Ferraro, 2005: Microwave rainfall estimation over coasts. *J. Atmos. and Oceanic Technol.* **22**, 497-512.

- Meneghini, R., T. Iguchi, T. Koizu, L. Liao, K. Okamoto, J. A. Jones, J., Kwiatkowski, 2000: Use of the surface reference technique for path attenuation estimates from the TRMM precipitation radar. *J. Appl. Meteor.*, **39**, 2053-2070.
- Oki, R., and A. Sumi, 1994: Sampling simulation of TRMM rainfall estimation using radar-AMeDAS composites. *J Appl. Meteor.*, **33**, 1597-1608.
- Olson, W. S., and Co-authors, 2006: Precipitation and latent heating distributions from satellite passive microwave radiometry. Part I: Improved method and uncertainty estimates. *J. Appl. Meteor.*, 702-720.
- Rosenfeld, D., D. Atlas and D. B. Wolff and E. Amitai, 1992: Beamwidth effects on Z-R relations and area integrated rainfall. *J. Appl. Meteor.*, **32**, No. 1, 50-72.
- Rosenfeld, D., D. B. Wolff and D. Atlas, 1993: General probability matched relations between radar reflectivity and rain rate. *J. Appl. Meteor.*, **31**, No. 5, 454-464.
- Rosenfeld, D., D. B. Wolff, and E. Amitai, 1994: The window probability matching method for rainfall measurements with radar. *J. Appl. Meteor.*, **33**, 682-693.
- Rosenfeld D., E. Amitai, and D. B. Wolff, 1995a: Classification of rain regimes by the three-dimensional properties of reflectivity fields. *J. Appl. Meteor.*, **34**, 198-211.

- Rosenfeld, D., E. Amitai and D. B. Wolff 1995: Improved accuracy of radar WPMM estimated rainfall upon application of objective classification criteria with radar. *J. Appl. Meteor.*, **34**, 212-223.
- Shin, K., and G. R. North, 1988: Sampling error study for rainfall estimate by satellite using a stochastic model. *J. Appl. Meteor.*, **27**, 1218-1231.
- Silberstein, D. S., D. B. Wolff, D. A. Marks, and J. L. Pippitt, 2005: Using ground clutter to adjust relative radar calibration at Kwajalein, RMI. *Preprints, 32<sup>nd</sup> Conference on Radar Meteorology, 3R.2, AMS, Albuquerque, NM, October 24-29, 2005.*
- Simpson, J., R. F. Adler, G. R. North, 1988: A proposed tropical rainfall measuring mission (TRMM) satellite. *Bull. Amer. Meteor. Soc.*, **69**, 278-294.
- Spencer, R., W. H. Goodman, and R. E. Hood, 1989: Precipitation retrieval over land and ocean with the SSM/I: identification and characteristics of the scattering signal. *J. Appl. Meteor.*, **6**, 254-273.
- Short, D. A., D. B. Wolff, D. Rosenfeld, and D. Atlas, 1993: A study of the threshold method utilizing rain gauge data. *J. Appl. Meteor.*, **32**, No. 8, 1379-1387.

- E. F. Stocker, J. Kwiatkowski and O. Kelley. 2001. Gridded Hourly Text Products: A TRMM Data Reduction Approach. Proceedings of IEEE 2001 International Geoscience and Remote Sensing Symposium. Sydney, Australia. pp. 658-660.
- Tao, W.-K., and J. Simpson, 1993: Goddard Cumulus Ensemble Model. Part I: Model description. *Terr. Atmos. Oceanic Sci.*, **4**, 35-72.
- Thiele, O., 1988: Validating Space Observations of Rainfall. *Tropical Rainfall Measurements*, J. S. Theon and N. Fugono, Eds., A. Deepak Publishing, 415-423.
- Wilheit, T. T., A. Chang, L. Chiu, 1991: Retrieval of monthly rainfall indices from microwave radiometric measurements using probability distribution function. *J. Atmos. Oceanic Technol.*, **8**, 118-136.
- Wilheit, T., C. Kummerow and R. Ferraro, 2003: Rainfall algorithms for AMSR-E, *IEEE: Trans. Geoscience & Rem. Sensing*, **41**, 204-214.
- Wolff, D. B., D. A. Marks, E. Amitai, D. S. Silberstein, B. L. Fisher, A. Tokay, J. Wang, and J. L. Pippitt, 2005: Ground validation for the Tropical Rainfall Measuring Mission (TRMM). *J. Atmos. Oceanic Technol.*, **22**, 365-380.
- Yuter, S., M. Miller, J. Stout, R. Wood, J. Kwiatkowski, D. Horn, and C. Spooner, 2006: Remaining challenges in satellite precipitation estimation for the Tropical Rainfall

Measuring Mission. Preprints, 4th European Conference on Radar in Meteorology and Hydrology. 18-22 September 2006, Barcelona, Spain.



## List of Figures

Fig. 1: Map illustrating the gauge and radar networks at GV sites: Darwin, Australia (DARW), Houston, Texas (HSTN), Kwajalein, Republic of the Marshall Islands (KWAJ) and Melbourne, Florida (MELB). Rings show distance from GV radar at increments of 50 km.

Fig. 2: Illustration of land/coast/ocean  $1/6^{\text{th}}$  degree mask used by the Version 6 TMI algorithm for each GV site. Shaded regions show TMI Version 6 surface mask of land (dark gray), coast (medium gray) and ocean (light gray). Also shown are the more subjectively classified  $0.5^{\circ} \times 0.5^{\circ}$  used for comparison of the GV data with the TRMM 3G68 product. Two character provides a GV coverage (F denotes full GV coverage, P is for partial), and geo-type of (L) land, (C) coast, and (O) for ocean.

Fig. 3: Mean monthly rain intensities (mm/hr) for GV (solid), PR (dot), COM (dash-dot) and TMI (dash) using  $0.5^{\circ}$  resolution for the period 1999-2004 at KWAJ.

Fig. 4: Same as Fig. 3, except for MELB (ocean only).

Fig. 5: Same as Fig. 3, except for MELB over land only.

Fig. 6: Same as Fig. 3, except for MELB over coast only.

Fig. 7: Probability Density Function (PDF) and Cumulative Distribution Frequency (CDF) of instantaneous rain rates ( $0.5^\circ$  resolution) for GV (solid), PR (dot), COM (dash-dot) and TMI (dash) as inferred from 3G68 products using  $0.5^\circ$  resolution for the period 1999-2004 at KWAJ.

Fig 8: Same as Fig. 7, except for MELB over ocean (left panel), coast (middle panel) and land (right panel).

Fig. 9: Illustration of a TRMM overpass of the KWAJ GV sites on 10/07/1999 showing the Level II rain data at each instrument's native resolution: top left panel (GV  $2\text{ km} \times 2\text{ km}$ ; top right panel (TMI  $\sim 150\text{ km}^2$  resolution); bottom left panel (PR  $4\text{ km}$  at nadir); and bottom right panel (COM  $4\text{ km}$  at nadir).

Fig. 10: Same as Fig. 9, except the GV, PR and COM data have been averaged within each TMI footprint.

Fig. 11: Top two panels display scatter plots of TMI (black), PR (blue) and COM (red) mean rain intensities versus mean rain intensities of the GV radar for KWAJ (top left) and MELB (top right). Note that satellite values are computed relative to the GV rain rate for each matching pixel and represent the statistical average at  $1\text{ mm/hr}$  intervals from  $0$  to  $40\text{ mm/hr}$ . Lower two panels display the estimated satellite errors of the TMI, PR and COM rain rate profiles for KWAJ (lower left) and MELB (lower left) as a function of the

GV rain intensity ranging from 0 to 35 mm/hr. Each profile was then smoothed using a three point averaging filter.

Fig. 12: Shows results for MELB displayed in Fig 11 stratified according to TMI  $1/6^{\text{th}}$  degree mask (Ocean, Land, Coast). The first column of scatter plots displays the satellite versus GV means as described in Fig. 11, whereas the second column of plots displays the estimated satellite errors as a function of the GV mean rain rate profile.

Fig. 13: PDF and CDF of rain rates for GV (solid), PR (dot), COM (dash-dot) and TMI (dash) estimates using  $0.5^{\circ}$  resolution for the period 1999-2004 at KWAJ at the TMI footprint scale.

Fig. 14: Sub-setted classification of KWAJ using a rough estimate of the TMI Version 5 surface mask, which considered the areas near the atolls to be coastal.

Fig. 15: PDF and CDF rain rates at KWAJ over gray area shown in Fig. 14 (top left panel), white area in Fig. 14 (middle panel) and all areas (same as in Fig. 13).

Fig. 16: PDF of TMI rain rates over  $2.5^{\circ} \times 2.5^{\circ}$  boxes over ocean (top left), land (middle) and coast (right). Data are color-coded by month and year and the ensemble. The dashed red lines represents August, 2001, which corresponds to the period during the TRMM boost from 350 km to 402 km. Data displayed in figure was obtained from Dr. Thomas Bell (NASA GSFC).

Fig. 17: PDF and CDF of rain rates at MELB at the TMI footprint scale for the period 1999-2004 showing GV (solid), PR (dot), COM (dash-dot) and TMI (dash). Top left panel shows the full GV area; top right panel is for ocean areas only; bottom left panel is for land areas only, and the bottom right is for land areas only.

Fig. 18: Same as Fig. 18, except for HSTN.

*Table 1: The number of  $1/6^\circ$  pixels and percentages (in apostrophes) of geographical types, via the TRMM TMI Version 6 algorithm, as a function of sampling area: Global represents  $\pm 70^\circ$  latitude; TRMM area is  $\pm 35^\circ$  latitude, Deep Tropics is  $\pm 10^\circ$ . Also shown are the respective percentages of geo-types at the four GV sites. Note that all GV sites except KWAJ have significant  $z$  coastal area, limiting the usefulness of comparisons to passive microwave estimates.*

<i>Area</i>	<i>Ocean</i>	<i>Land</i>	<i>Coast</i>	<i>Other</i>	<i>Total</i>
				543055	
<i>Global</i>	952643 (40.8)	682813 (29.3)	154289 (6.6)	(23.3)	2332800
<i>TRMM</i>	646298 (71.2)	217582 (24.0)	43044 (4.7)	276 (0.0)	907200
<i>Deep Tropics</i>	191754 (74.0)	51275 (19.8)	16171 (6.2)	~	259200
<i>KWAJ</i>	441 (100.0)	~	~	~	441
<i>MELB</i>	112 (41.5)	72 (26.7)	86 (31.9)	~	270
<i>HSTN</i>	90 (27.8)	153 (47.2)	81 (25.0)	~	324
<i>DARW</i>	104 (27.5)	104 (27.5)	170 (45.0)	~	378

Table 2: Statistics for 3G68 comparison for KWAJ, HSTN and MELB showing site, year, mean rain rates (GV, PR, TMI and COM), as well as the GV-relative biases.

Site	Year	Type	GV Mean	PR Mean	TMI Mean	COM Mean	PR Bias	TMI Bias	COM Bias
HSTN	1999	FL	0.0671	0.0634	0.0787	0.0829	-5.5	17.4	23.5
HSTN	2000	FL	0.0806	0.0861	0.0983	0.1245	6.9	22	54.5
HSTN	2001	FL	0.1863	0.1514	0.2387	0.1959	-18.8	28.1	5.2
HSTN	2002	FL	0.2517	0.2065	0.1987	0.3073	-17.9	-21	22.1
HSTN	2003	FL	0.1302	0.0835	0.1183	0.1019	-35.9	-9.2	-21.7
HSTN	2004	FL	0.1905	0.1663	0.199	0.1806	-12.7	4.4	-5.2
<b>HSTN</b>	<b>1999-2004</b>	<b>FL</b>	<b>0.1527</b>	<b>0.127</b>	<b>0.1563</b>	<b>0.1661</b>	<b>-16.8</b>	<b>2.4</b>	<b>8.8</b>
HSTN	1999	FC	0.0901	0.0871	0.0778	0.121	-3.3	-13.7	34.4
HSTN	2000	FC	0.0712	0.0727	0.0532	0.0972	2.1	-25.3	36.5
HSTN	2001	FC	0.1604	0.1399	0.165	0.1888	-12.8	2.8	17.7
HSTN	2002	FC	0.2716	0.212	0.2184	0.2476	-21.9	-19.6	-8.8
HSTN	2003	FC	0.1138	0.1069	0.1255	0.131	-6.1	10.3	15.1
HSTN	2004	FC	0.096	0.1106	0.096	0.1615	15.2	0	68.2
<b>HSTN</b>	<b>1999-2004</b>	<b>FC</b>	<b>0.1341</b>	<b>0.122</b>	<b>0.1233</b>	<b>0.1585</b>	<b>-9</b>	<b>-8</b>	<b>18.2</b>
HSTN	1999	FO	0.0591	0.0655	0.0402	0.0783	10.8	-31.9	32.6
HSTN	2000	FO	0.0776	0.0577	0.0698	0.0719	-25.6	-10	-7.3
HSTN	2001	FO	0.2404	0.1662	0.206	0.241	-30.9	-14.3	0.2
HSTN	2002	FO	0.3593	0.36	0.3218	0.4194	0.2	-10.4	16.7
HSTN	2003	FO	0.1409	0.1195	0.1115	0.1231	-15.2	-20.9	-12.7
HSTN	2004	FO	0.1617	0.0881	0.0822	0.1179	-45.5	-49.2	-27.1
<b>HSTN</b>	<b>1999-2004</b>	<b>FO</b>	<b>0.174</b>	<b>0.1429</b>	<b>0.1386</b>	<b>0.1752</b>	<b>-17.8</b>	<b>-20.3</b>	<b>0.7</b>
MELB	1999	FL	0.1923	0.1806	0.2069	0.2239	-6.1	7.6	16.4
MELB	2000	FL	0.0838	0.068	0.0743	0.0822	-18.9	-11.3	-1.9
MELB	2001	FL	0.0971	0.093	0.0993	0.1175	-4.3	2.2	21
MELB	2002	FL	0.1814	0.1582	0.1766	0.2052	-12.8	-2.6	13.1
MELB	2003	FL	0.2194	0.2142	0.2778	0.2769	-2.4	26.6	26.2
MELB	2004	FL	0.1266	0.1228	0.1538	0.1592	-2.9	21.5	25.8
<b>MELB</b>	<b>1999-2004</b>	<b>FL</b>	<b>0.1516</b>	<b>0.1409</b>	<b>0.167</b>	<b>0.1795</b>	<b>-7</b>	<b>10.2</b>	<b>18.4</b>
MELB	1999	FC	0.1541	0.1426	0.1232	0.1705	-7.4	-20	10.7
MELB	2000	FC	0.1038	0.0817	0.0675	0.0956	-21.2	-34.9	-7.8
MELB	2001	FC	0.1256	0.1034	0.1054	0.1366	-17.7	-16.1	8.7
MELB	2002	FC	0.1542	0.1454	0.1412	0.181	-5.7	-8.4	17.4
MELB	2003	FC	0.1079	0.1106	0.1279	0.144	2.5	18.5	33.4
MELB	2004	FC	0.1135	0.1113	0.1136	0.1336	-1.9	0.1	17.7
<b>MELB</b>	<b>1999-2004</b>	<b>FC</b>	<b>0.1263</b>	<b>0.1161</b>	<b>0.1139</b>	<b>0.1439</b>	<b>-8.1</b>	<b>-9.9</b>	<b>13.9</b>
MELB	1999	FO	0.1369	0.1254	0.1164	0.1506	-8.4	-15	10.1
MELB	2000	FO	0.0873	0.089	0.0774	0.1046	2	-11.4	19.9
MELB	2001	FO	0.1199	0.1232	0.1118	0.1504	2.7	-6.8	25.4
MELB	2002	FO	0.13	0.1363	0.1194	0.164	4.9	-8.1	26.2
MELB	2003	FO	0.1098	0.1153	0.1071	0.1426	5	-2.5	29.8
MELB	2004	FO	0.0918	0.1115	0.087	0.1058	21.5	-5.1	15.4
<b>MELB</b>	<b>1999-2004</b>	<b>FO</b>	<b>0.1124</b>	<b>0.117</b>	<b>0.1032</b>	<b>0.1364</b>	<b>4.1</b>	<b>-8.2</b>	<b>21.3</b>
KWAJ	1999	FO	0.1651	0.1392	0.1459	0.1603	-15.7	-11.6	-2.9
KWAJ	2000	FO	0.2881	0.2571	0.2536	0.2817	-10.8	-12	-2.2
KWAJ	2001	FO	0.2149	0.1816	0.2071	0.1884	-15.5	-3.6	-12.3
KWAJ	2002	FO	0.2807	0.2621	0.2804	0.2744	-6.6	-0.1	-2.3
KWAJ	2003	FO	0.2379	0.2039	0.2431	0.2268	-14.3	2.2	-4.6

KWAJ	2004 FO	0.2269	0.174	0.1642	0.2027	-23.3	-27.6	-10.7
KWAJ	1999-2004 FO	0.2383	0.2055	0.2194	0.2247	-13.7	-7.9	-5.7

*Table 3: Number of TRMM overpasses and associated TMI footprints available for this study over the period 1999-2004, for each GV site.*

GV Site	No. <i>Overpasses</i>	<i>No. Footprints</i>			
		All	Ocean	Land	Coast
Kwajalein	257	70993	70993	0	0
Melbourne	236	54943	16875	16618	21450
Houston	260	61336	14223	29142	17971



Table 4 Melbourne regression parameters (A = All, O = Ocean, L = Land, C = Coast).

Satellite Product	TMI Surface Flag	RR Regime (mm/hr)	Regression Parameters		
			Intercept	R	Slope
TMI	A	0 - 20	2.03	0.98	0.45
PR	A	0 - 20	2.16	0.97	0.60
COM	A	0 - 20	1.37	1.00	0.76
TMI	O	0 - 20	2.32	0.97	0.44
PR	O	0 - 20	2.54	0.96	0.62
COM	O	0 - 20	1.69	0.99	0.69
TMI	L	0 - 20	1.89	0.97	0.53
PR	L	0 - 20	2.37	0.95	0.58
COM	L	0 - 20	1.35	0.97	0.84
TMI	C	0 - 20	2.12	0.95	0.37
PR	C	0 - 20	1.91	0.98	0.60
COM	C	0 - 20	1.45	0.99	0.74
TMI	A	21-40	7.94	0.59	0.24
PR	A	21-40	9.66	0.74	0.20
COM	A	21-40	3.06	0.85	0.70
TMI	O	21-40	9.41	0.23	0.09
PR	O	21-40	13.87	0.08	0.04
COM	O	21-40	2.22	0.53	0.61
TMI	L	21-40	10.85	0.40	0.26
PR	L	21-40	11.64	0.31	0.10
COM	L	21-40	8.36	0.69	0.56
TMI	C	21-40	3.63	0.62	0.35
PR	C	21-40	5.95	0.76	0.35
COM	C	21-40	-2.30	0.81	0.94

*Table 5 Kwajalein regression parameters (all pixels are classified as ocean)*

Satellite Product	TMI Surface Flag	RR Regime (mm/hr)	Regression Parameters		
			Intercept	R	Slope
TMI	O/A	0 - 20	2.39	0.95	0.41
PR	O/A	0 - 20	0.32	1.00	0.68
COM	O/A	0 - 20	1.03	0.99	0.50
TMI	O/A	21-40	4.27	0.79	0.27
PR	O/A	21-40	0.37	0.74	0.64
COM	O/A	21-40	-9.35	0.89	0.92

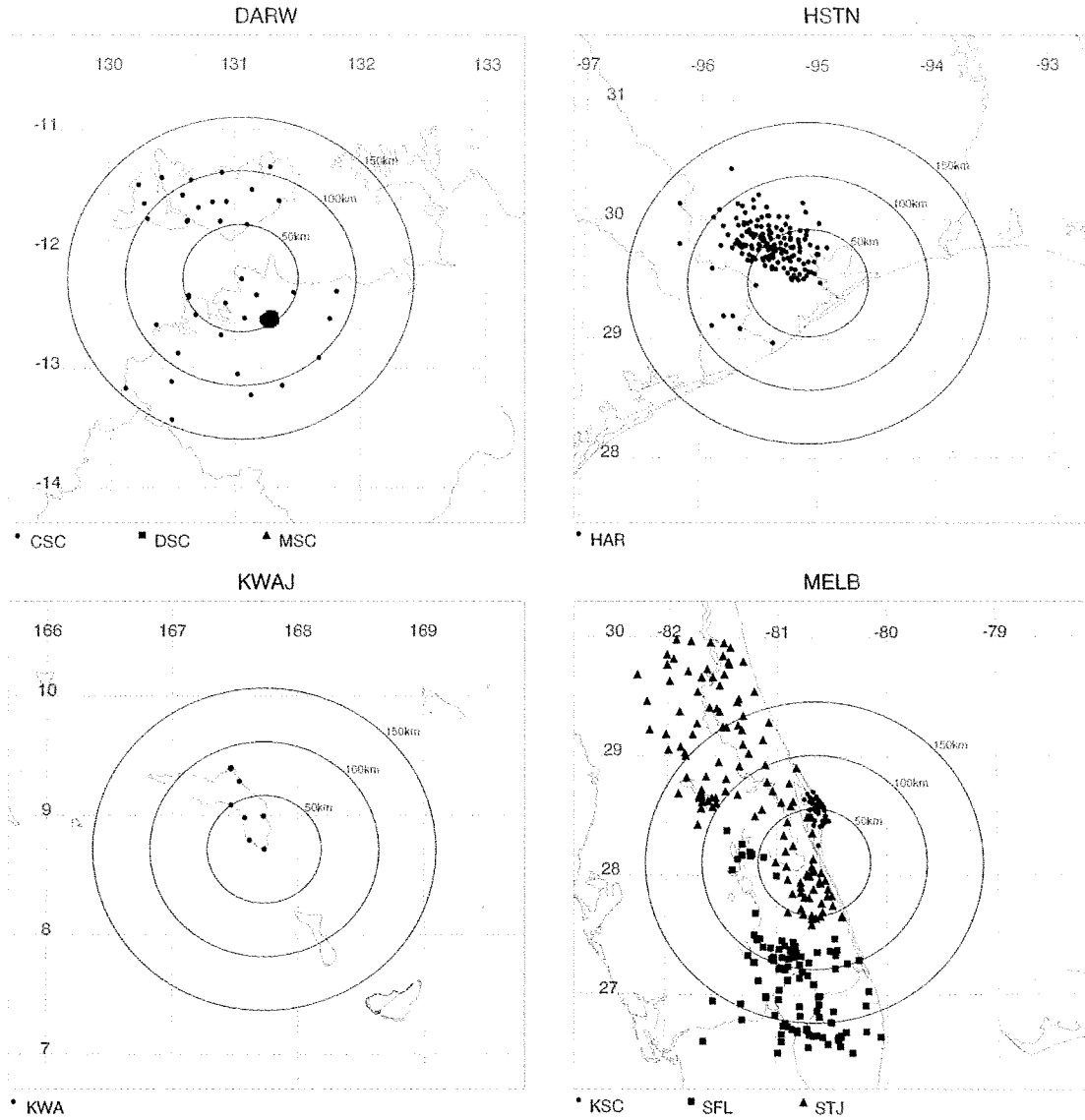


Fig. 1: Map illustrating the gauge and radar networks at GV sites: Darwin, Australia (DARW), Houston, Texas (HSTN), Kwajalein, Republic of the Marshall Islands (KWAJ) and Melbourne, Florida (MELB). Rings show distance from GV radar at increments of 50 km.

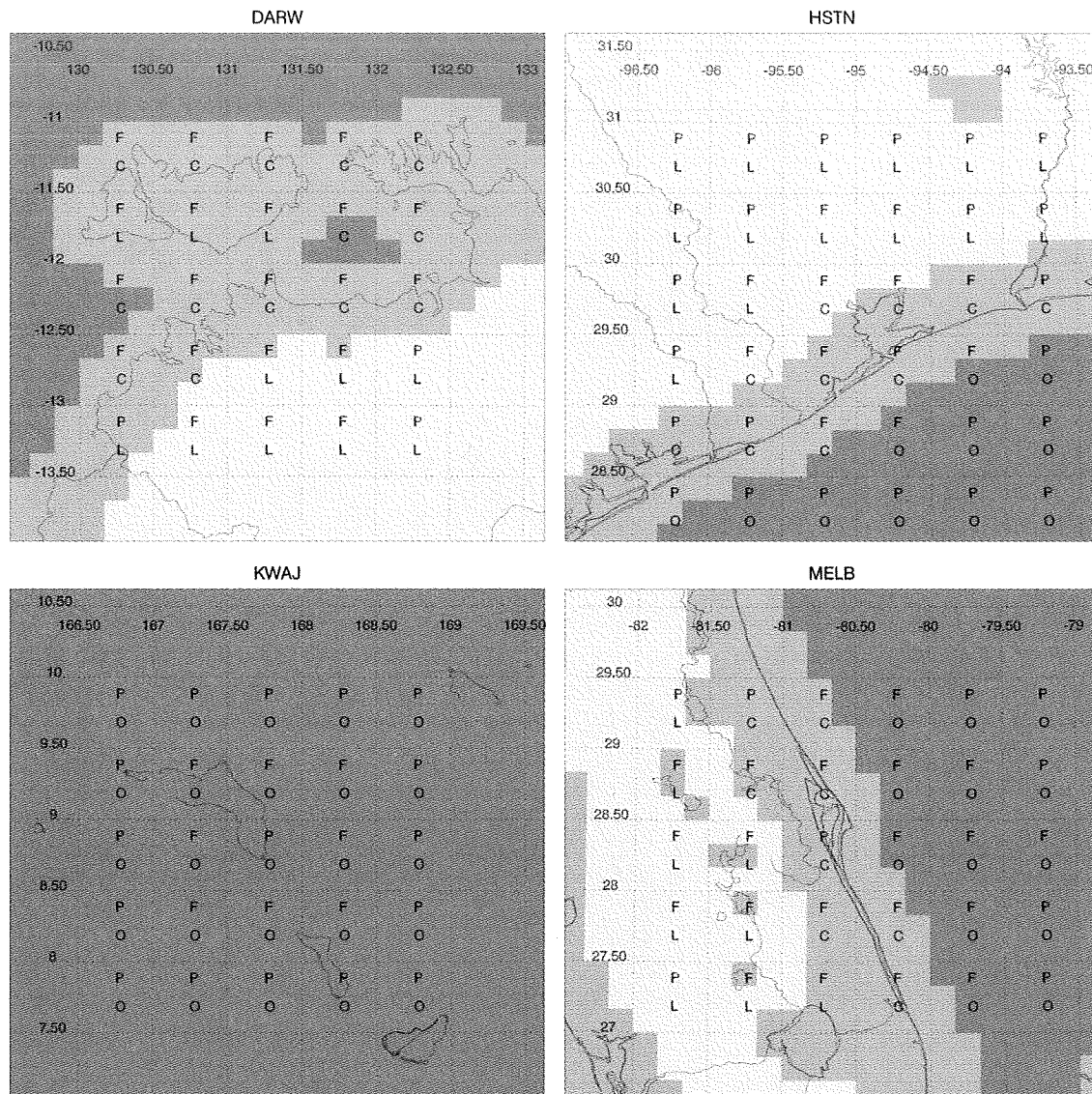


Fig. 2: Illustration of land/coast/ocean  $1/6^{\text{th}}$  degree mask used by the Version 6 TMI algorithm for each GV site. Shaded regions show TMI Version 6 surface mask of land (dark gray), coast (medium gray) and ocean (light gray). Also shown are the more subjectively classified  $0.5^{\circ} \times 0.5^{\circ}$  used for comparison of the GV data with the TRMM 3G68 product. Two character provides a GV coverage (F denotes full GV coverage, P is for partial), and geo-type of (L) land, (C) coast, and (O) for ocean.

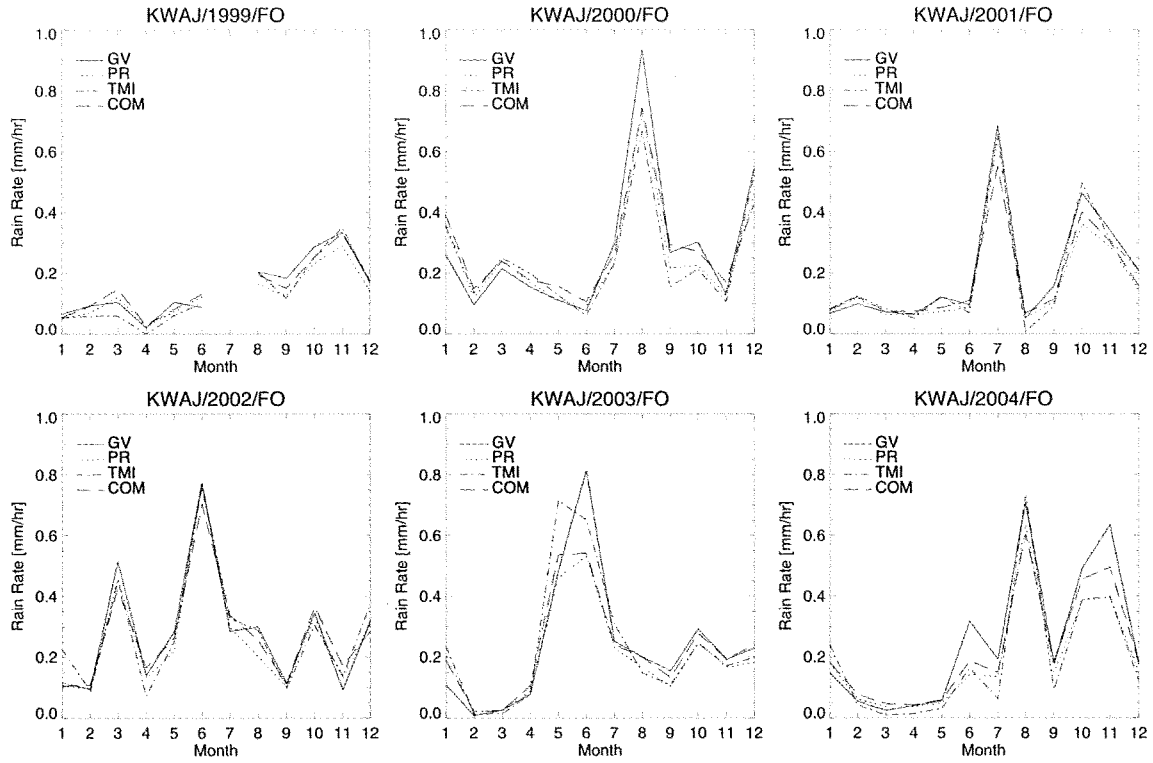


Fig. 3: Mean monthly rain intensities (mm/hr) for GV (solid), PR (dot), COM (dash-dot) and TMI (dash) using  $0.5^\circ$  resolution for the period 1999-2004 at KWAJ.

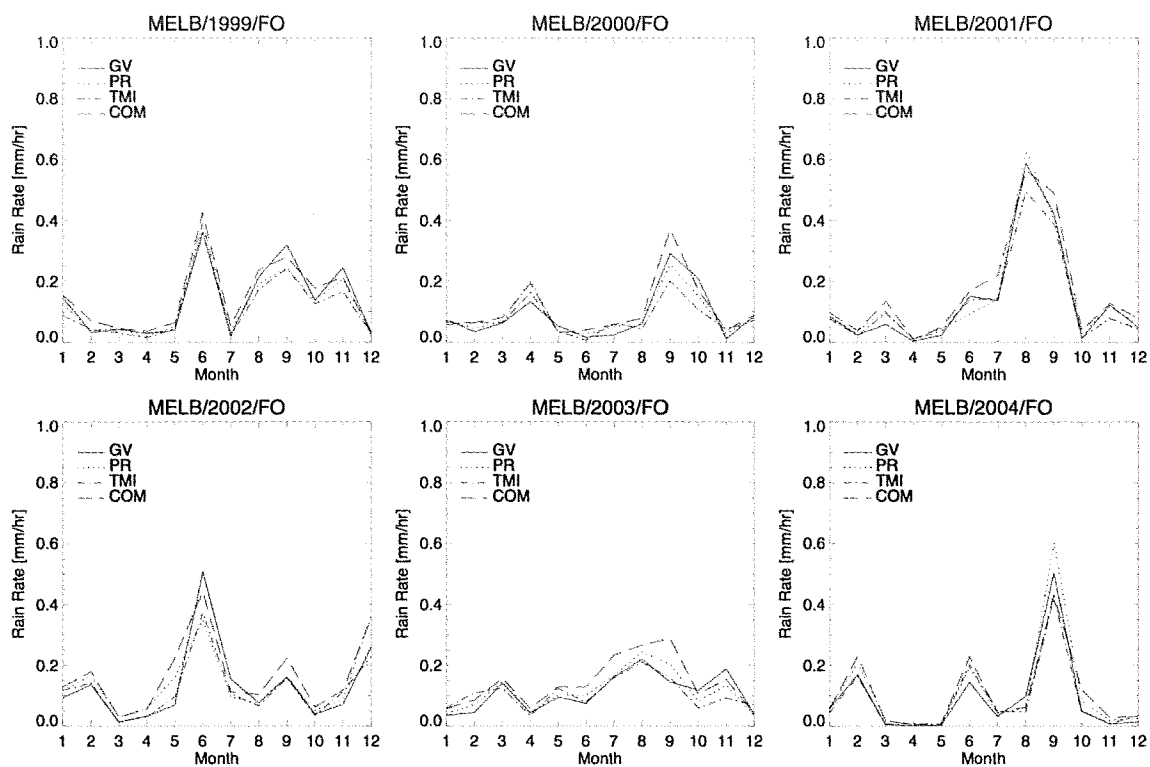


Fig. 4: Same as Fig. 3, except for MELB (ocean only).

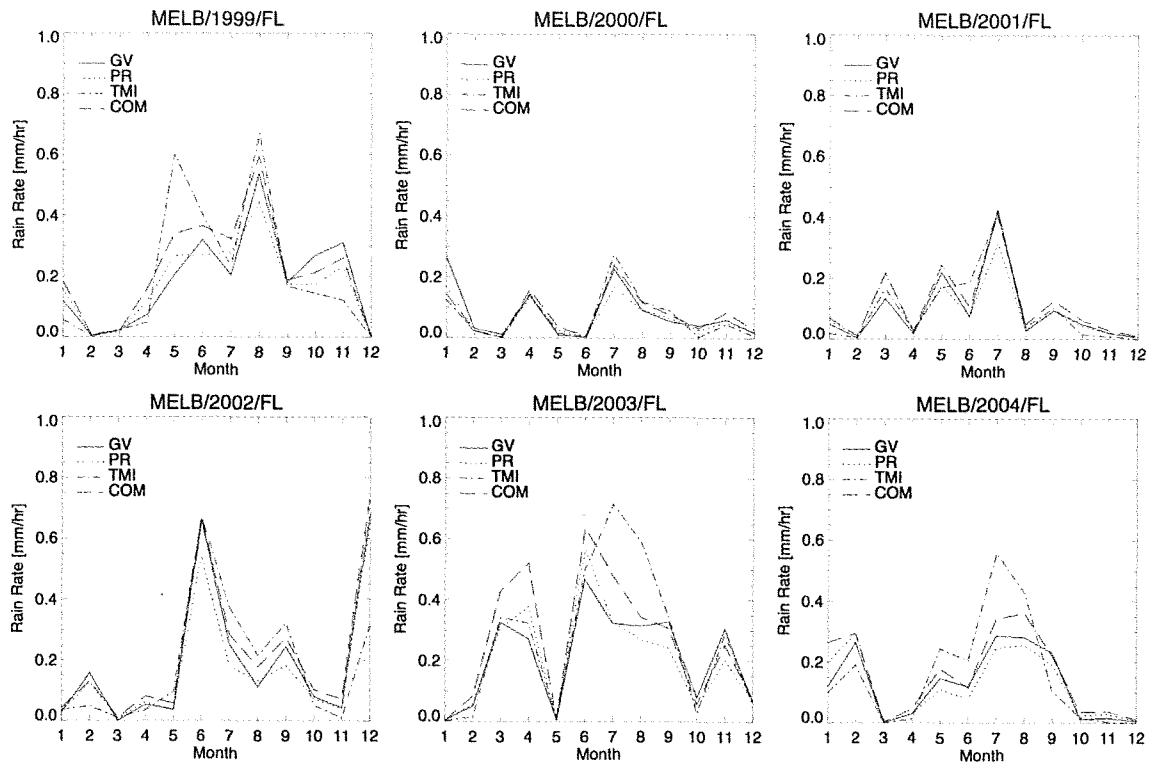


Fig. 5: Same as Fig. 3, except for MELB over land only.

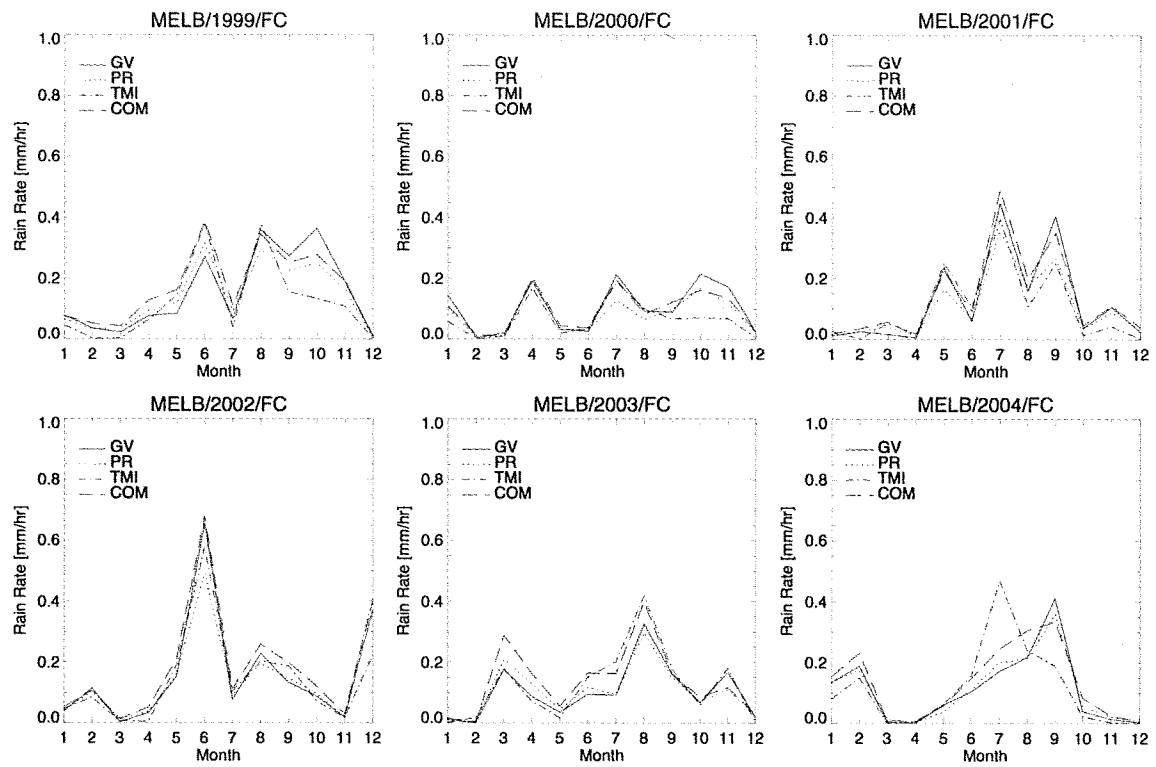


Fig. 6: Same as Fig. 3, except for MELB over coast only.



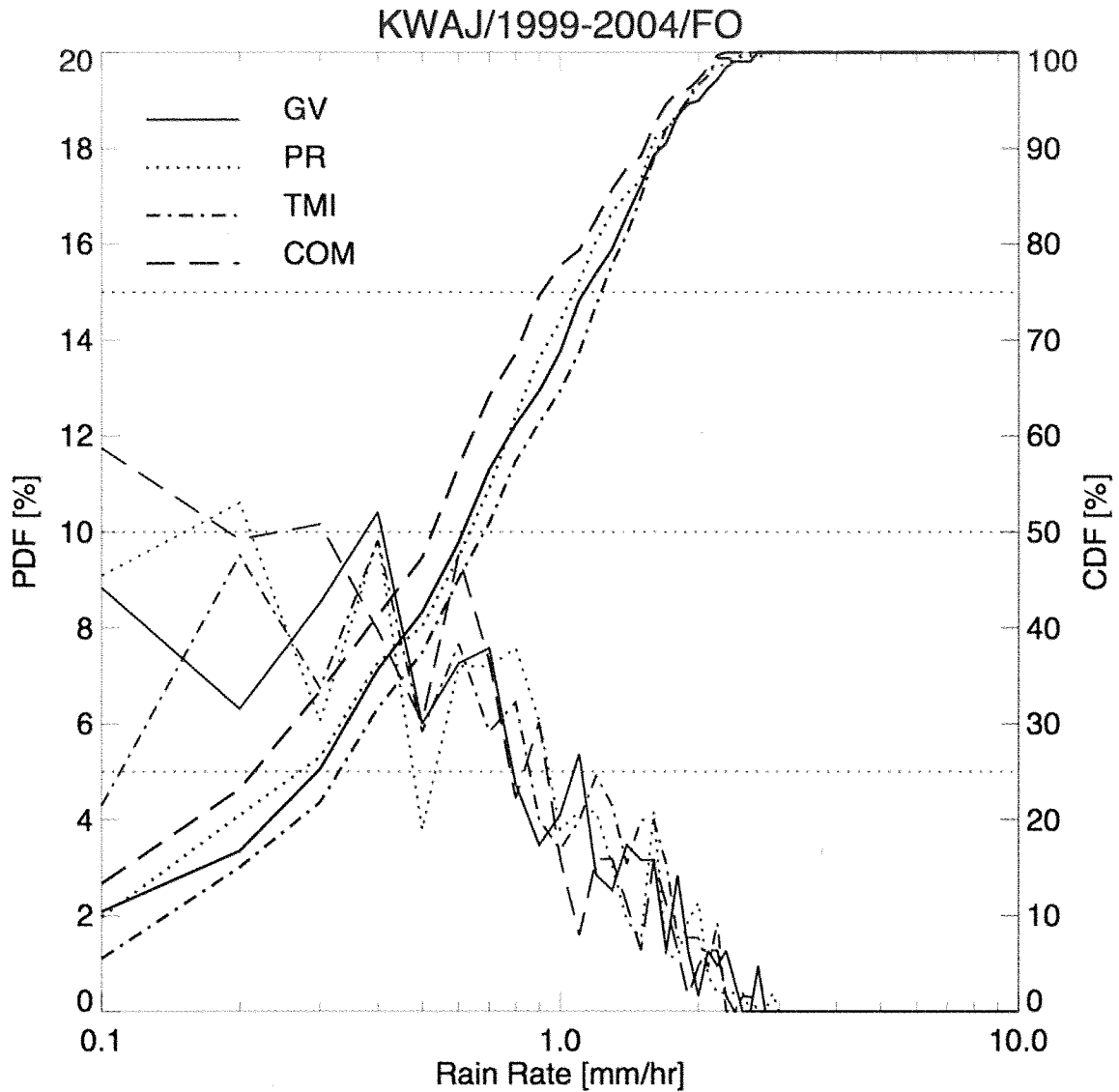


Fig. 7: Probability Density Function (PDF) and Cumulative Distribution Frequency (CDF) of instantaneous rain rates ( $0.5^\circ$  resolution) for GV (solid), PR (dot), COM (dash-dot) and TMI (dash) as inferred from 3G68 products using  $0.5^\circ$  resolution for the period 1999-2004 at KWAJ.

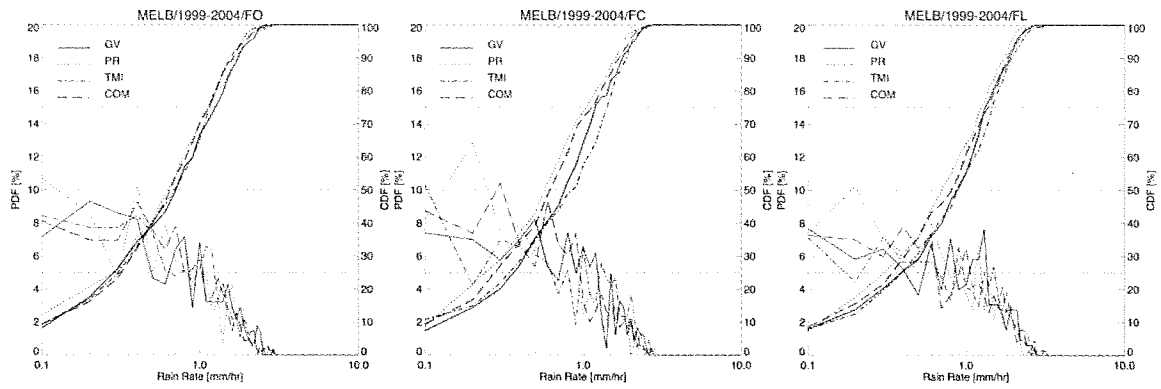


Fig 8: Same as Fig. 7, except for MELB over ocean (left panel), coast (middle panel) and land (right panel).

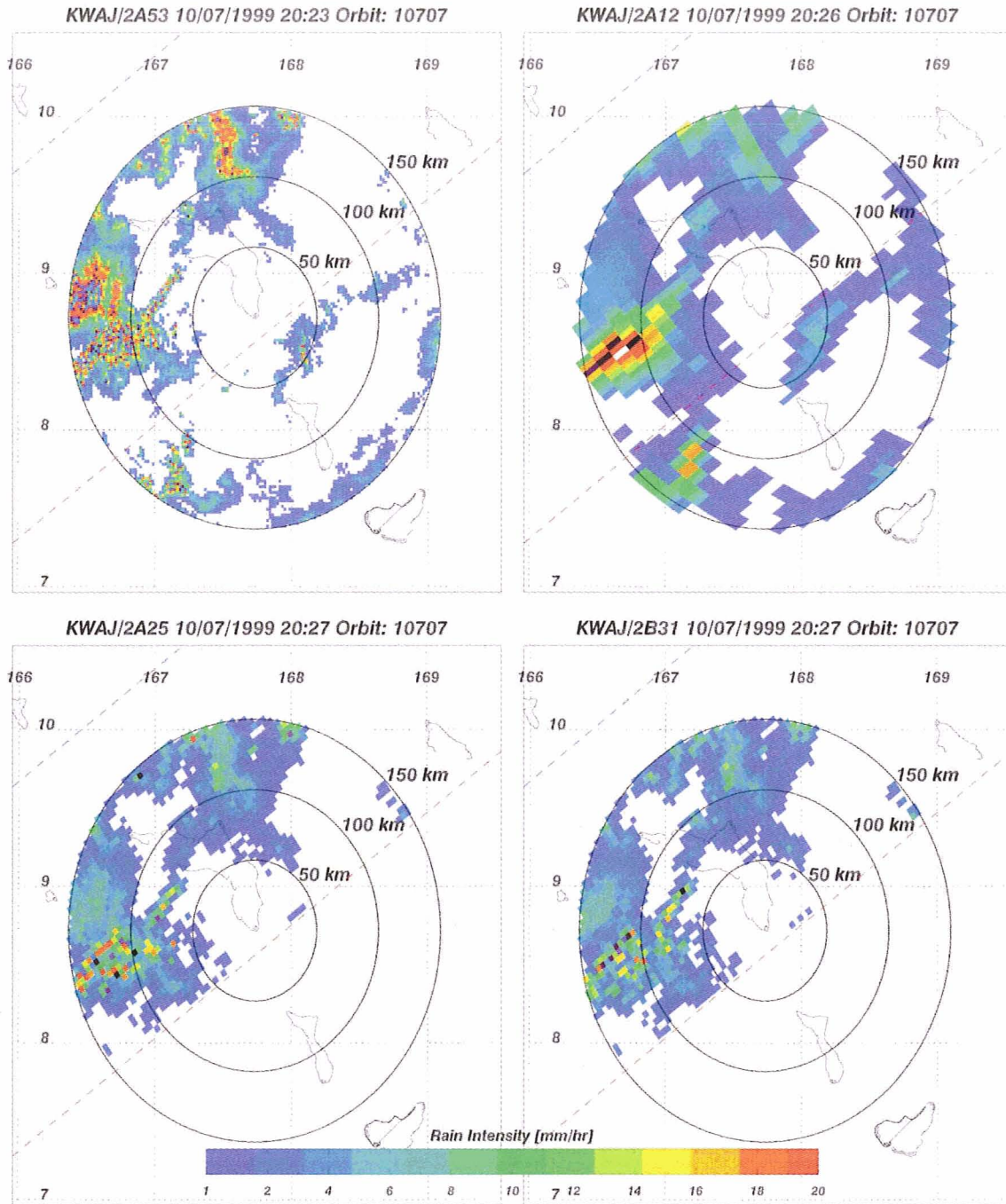


Fig. 9: Illustration of a TRMM overpass of the KWAJ GV sites on 10/07/1999 showing the Level II rain data at each instrument's native resolution: top left panel (GV 2 km x 2 km; top right panel (TMI ~150 km<sup>2</sup> resolution); bottom left panel (PR 4 km at nadir); and bottom right panel (COM 4 km at nadir).

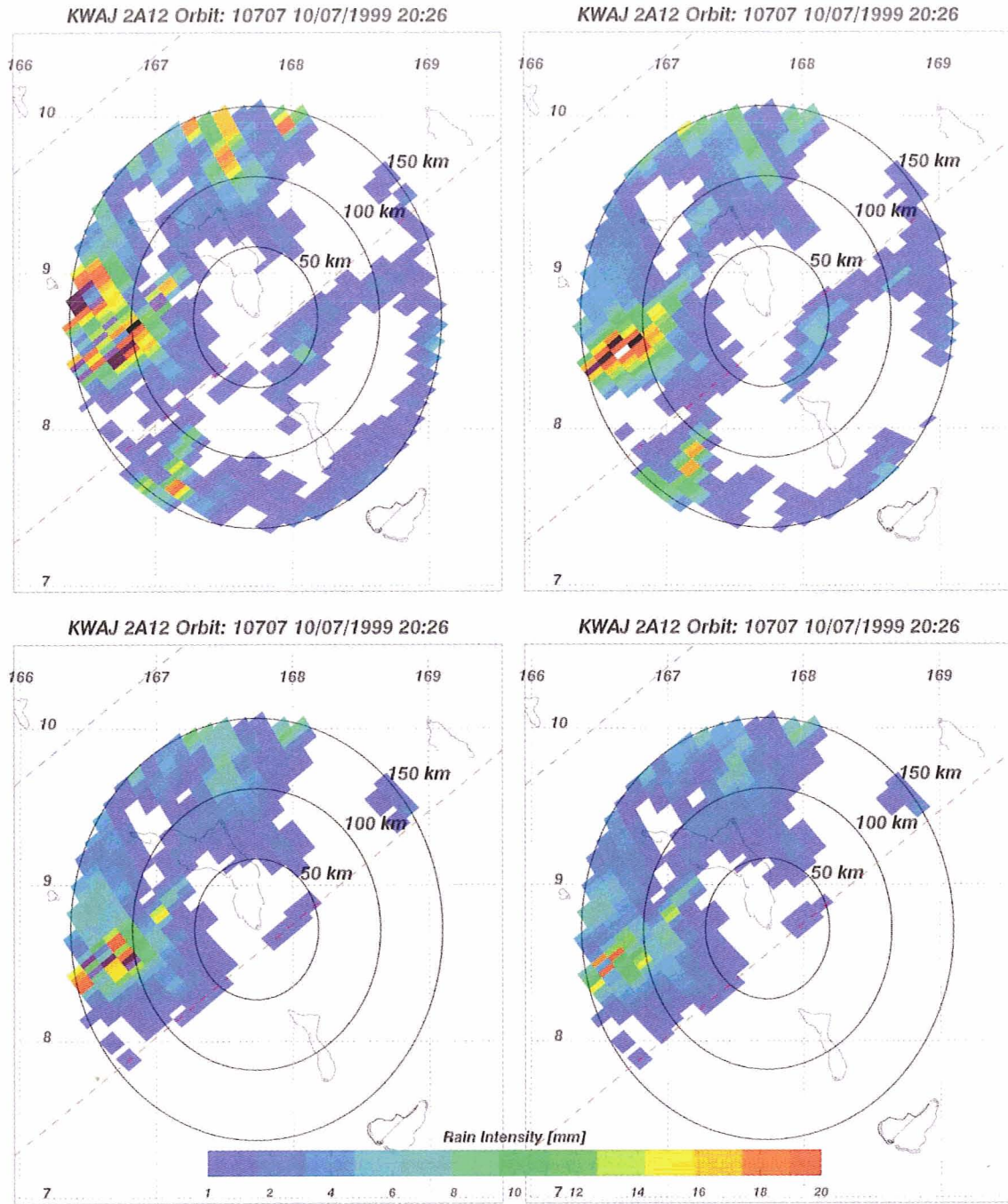


Fig. 10: Same as Fig. 9, except the GV, PR and COM data have been averaged within each TMI footprint.

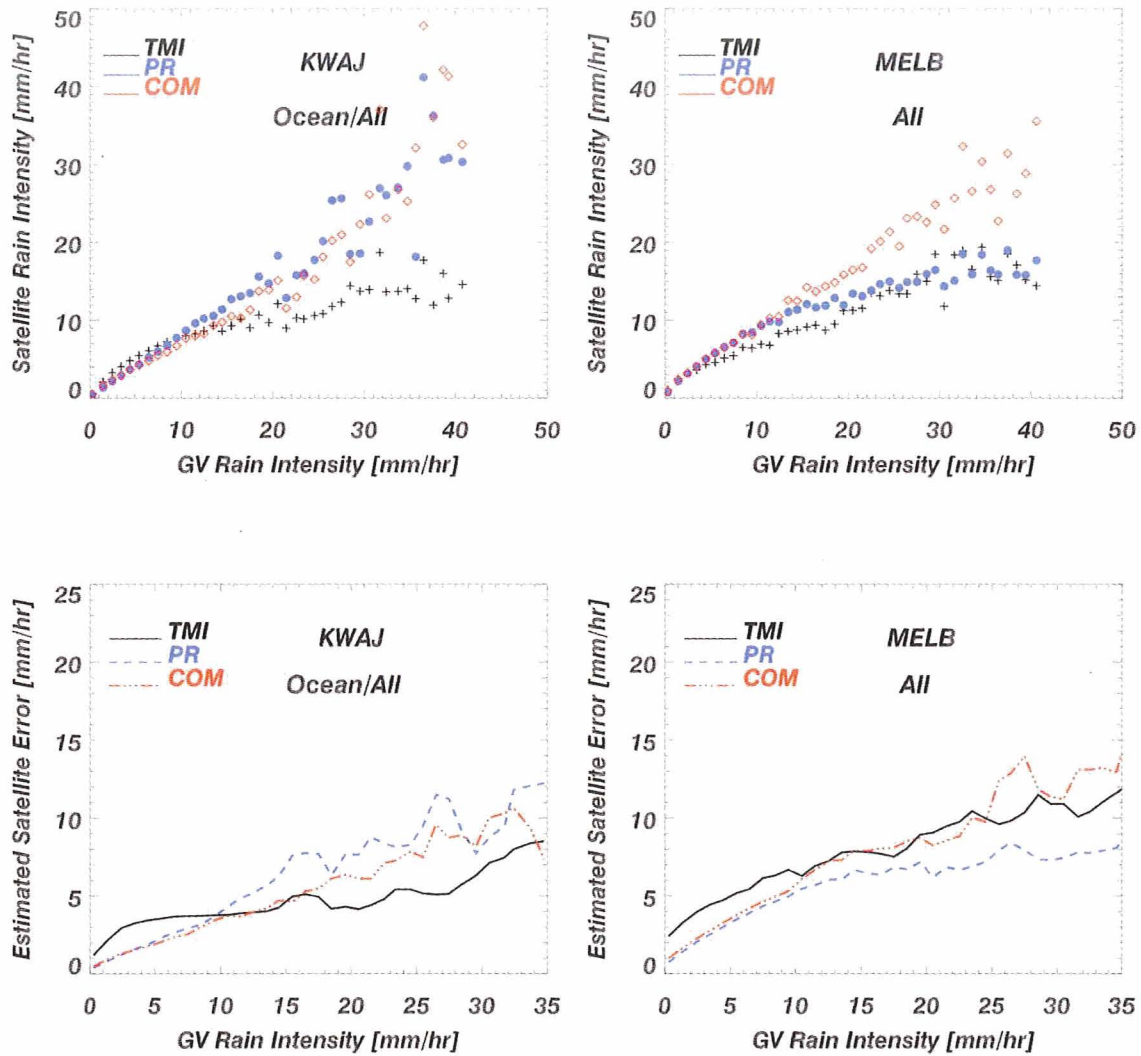


Fig. 11: Top two panels display scatter plots of TMI (black), PR (blue) and COM (red) mean rain intensities versus mean rain intensities of the GV radar for KWAJ (top left) and MELB (top right). Note that satellite values are computed relative to the GV rain rate for each matching pixel and represent the statistical average at 1 mm/hr intervals from 0 to 40 mm/hr. Lower two panels display the estimated satellite errors of the TMI, PR and COM rain rate profiles for KWAJ (lower left) and MELB (lower left) as a function of the GV rain intensity ranging from 0 to 35 mm/hr. Each profile was then smoothed using a three point averaging filter.



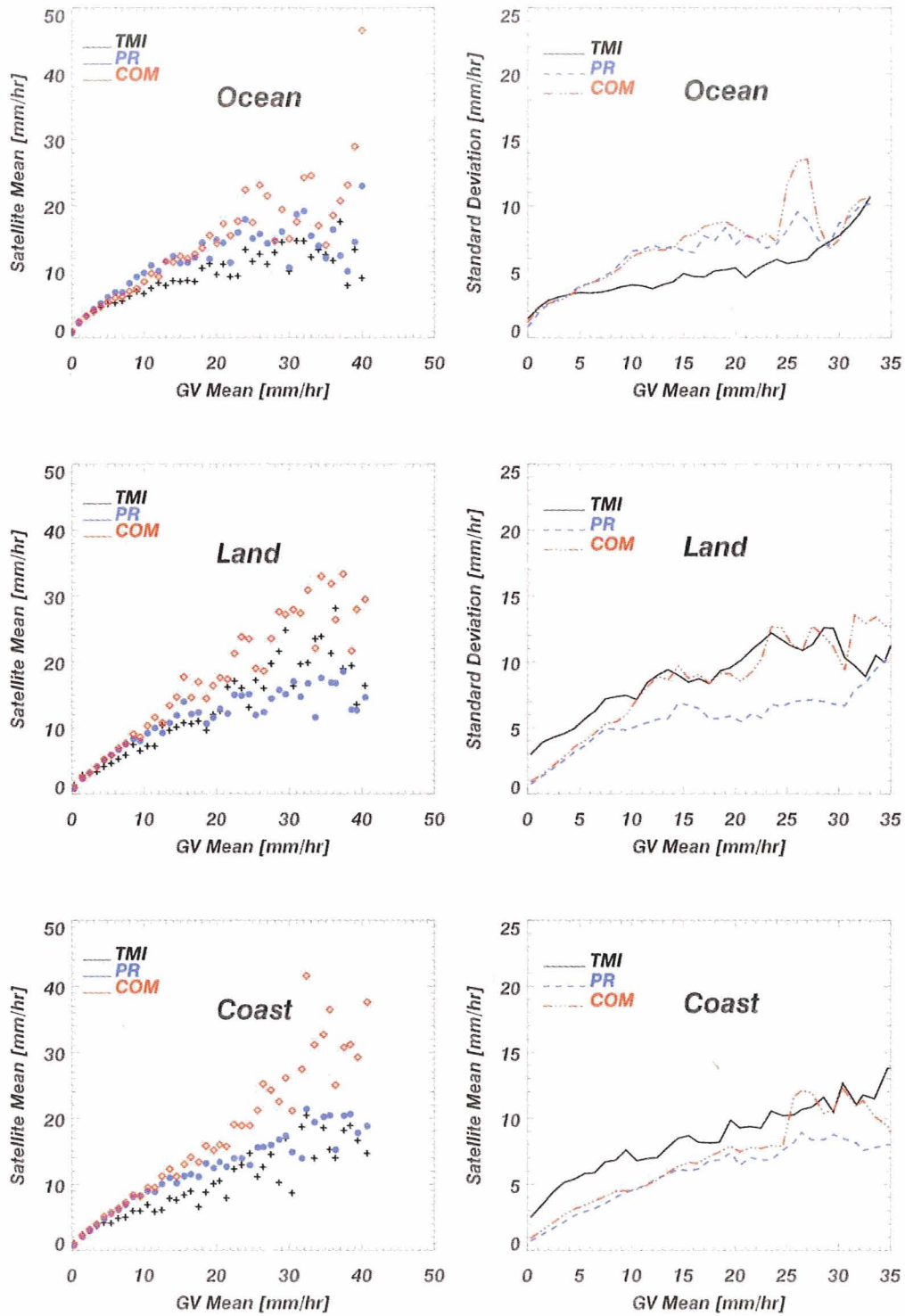


Fig. 12: Shows results for MELB displayed in Fig 11 stratified according to TMI 1/6<sup>th</sup> degree mask (Ocean, Land, Coast). The first column of scatter plots displays the satellite versus GV means as described in Fig. 11, whereas the second column of plots displays the estimated satellite errors as a function of the GV mean rain rate profile.

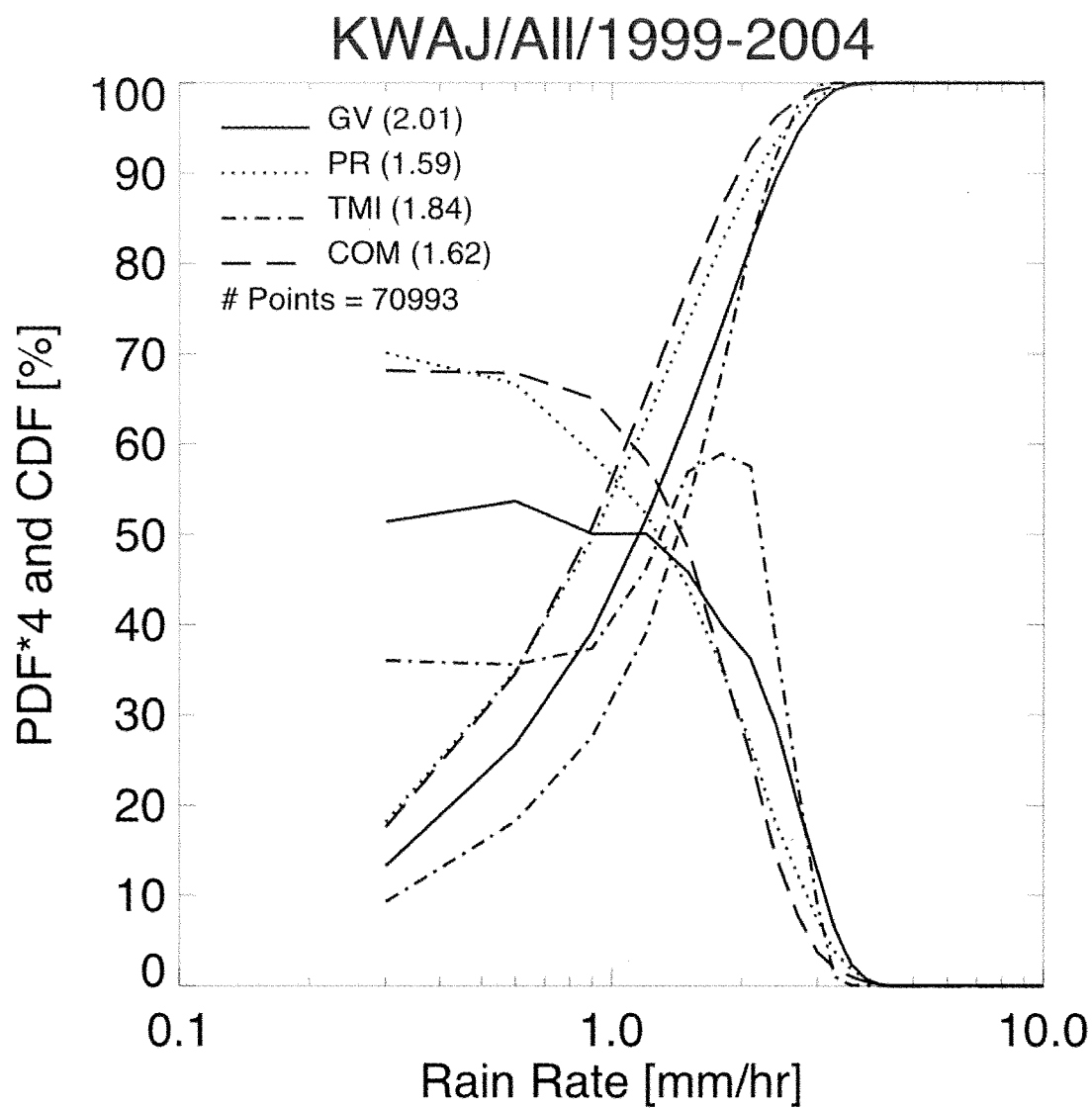


Fig. 13: PDF and CDF of rain rates for GV (solid), PR (dot), COM (dash-dot) and TMI (dash) estimates using  $0.5^\circ$  resolution for the period 1999-2004 at KWAJ at the TMI footprint scale.



Fig. 14: Sub-setted classification of KWAJ using a rough estimate of the TMI Version 5 surface mask, which considered the areas near the atolls to be coastal.



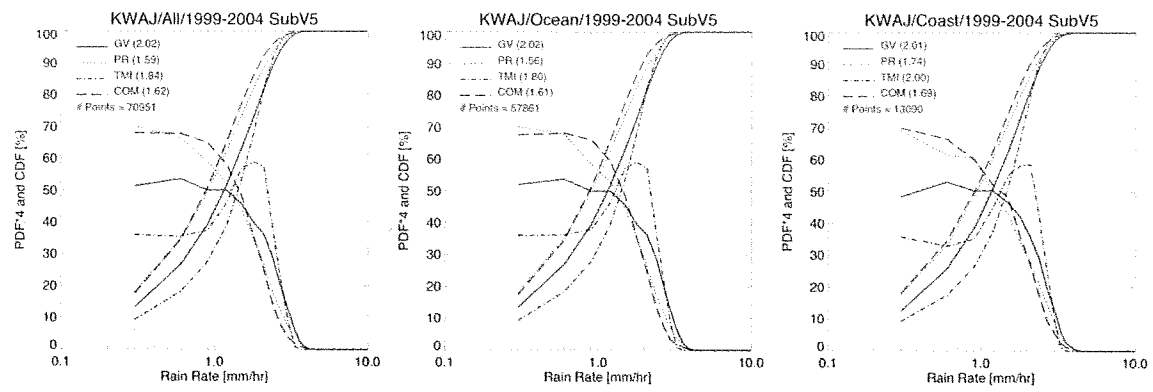


Fig. 15: PDF and CDF rain rates at KWAJ over gray area shown in Fig. 14 (top left panel), white area in Fig. 14 (middle panel) and all areas (same as in Fig. 13).

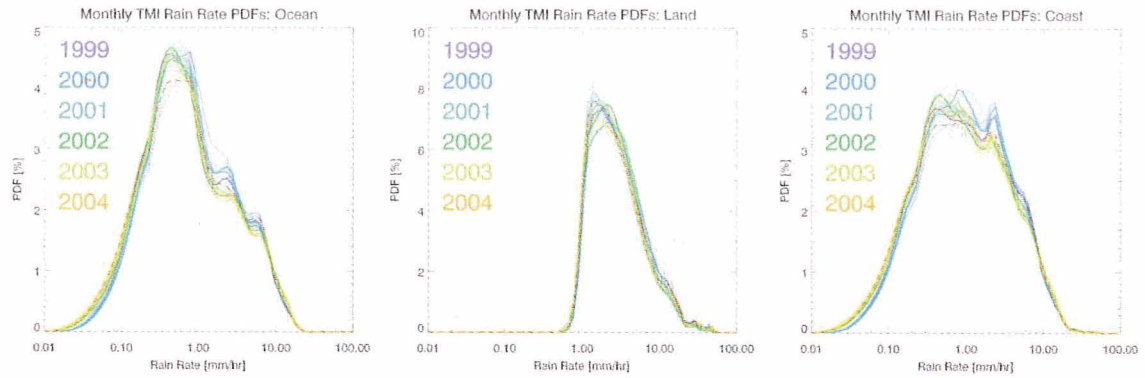


Fig. 16: PDF of TMI rain rates over  $2.5^\circ \times 2.5^\circ$  boxes over ocean (top left), land (middle) and coast (right). Data are color-coded by month and year and the ensemble. The dashed red lines represents August, 2001, which corresponds to the period during the TRMM boost from 350 km to 402 km. Data displayed in figure was obtained from Dr. Thomas Bell (NASA GSFC).

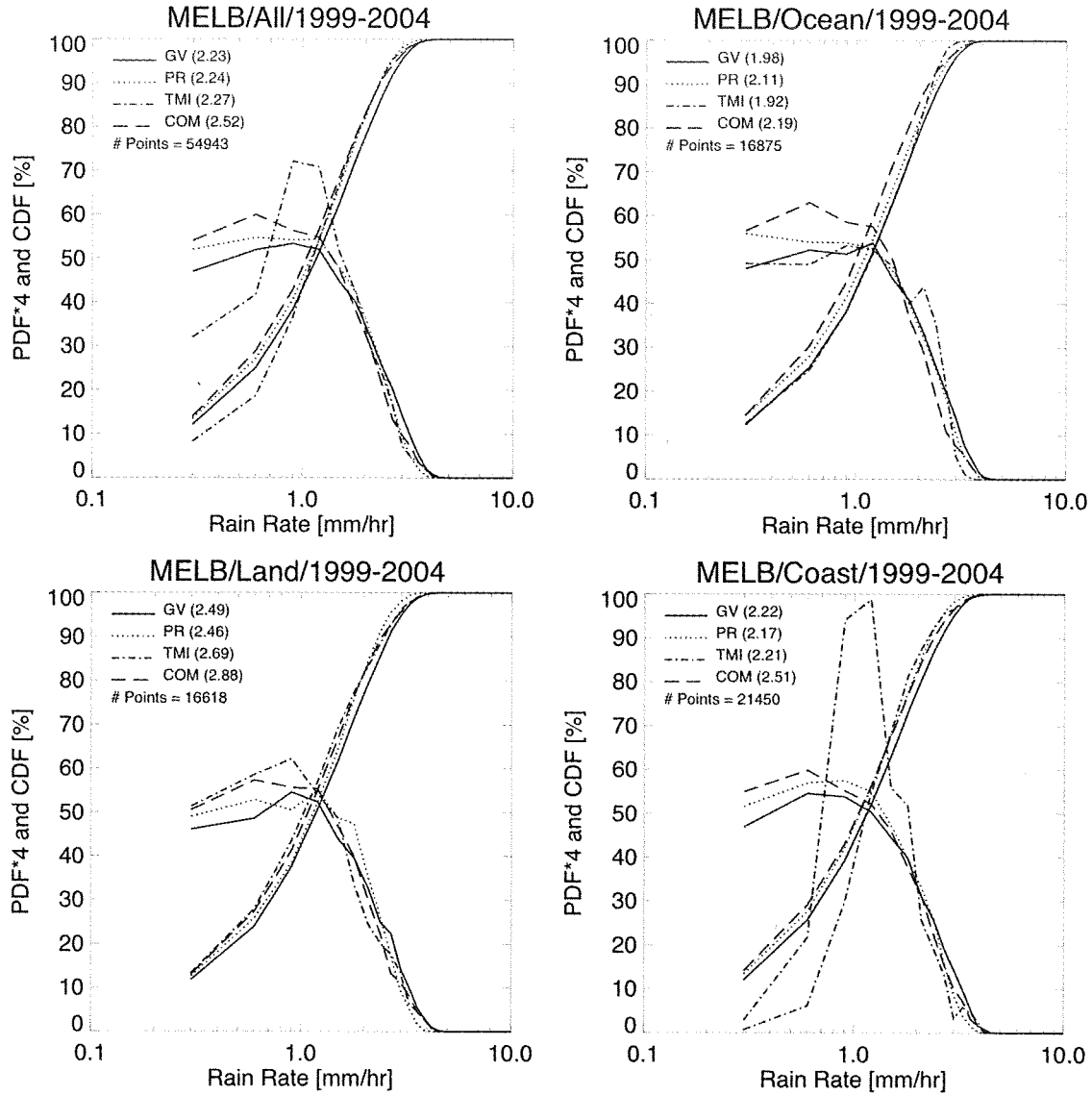


Fig. 17: PDF and CDF of rain rates at MELB at the TMI footprint scale for the period 1999-2004 showing GV (solid), PR (dot), COM (dash-dot) and TMI (dash). Top left panel shows the full GV area; top right panel is for ocean areas only; bottom left panel is for land areas only, and the bottom right is for land areas only.

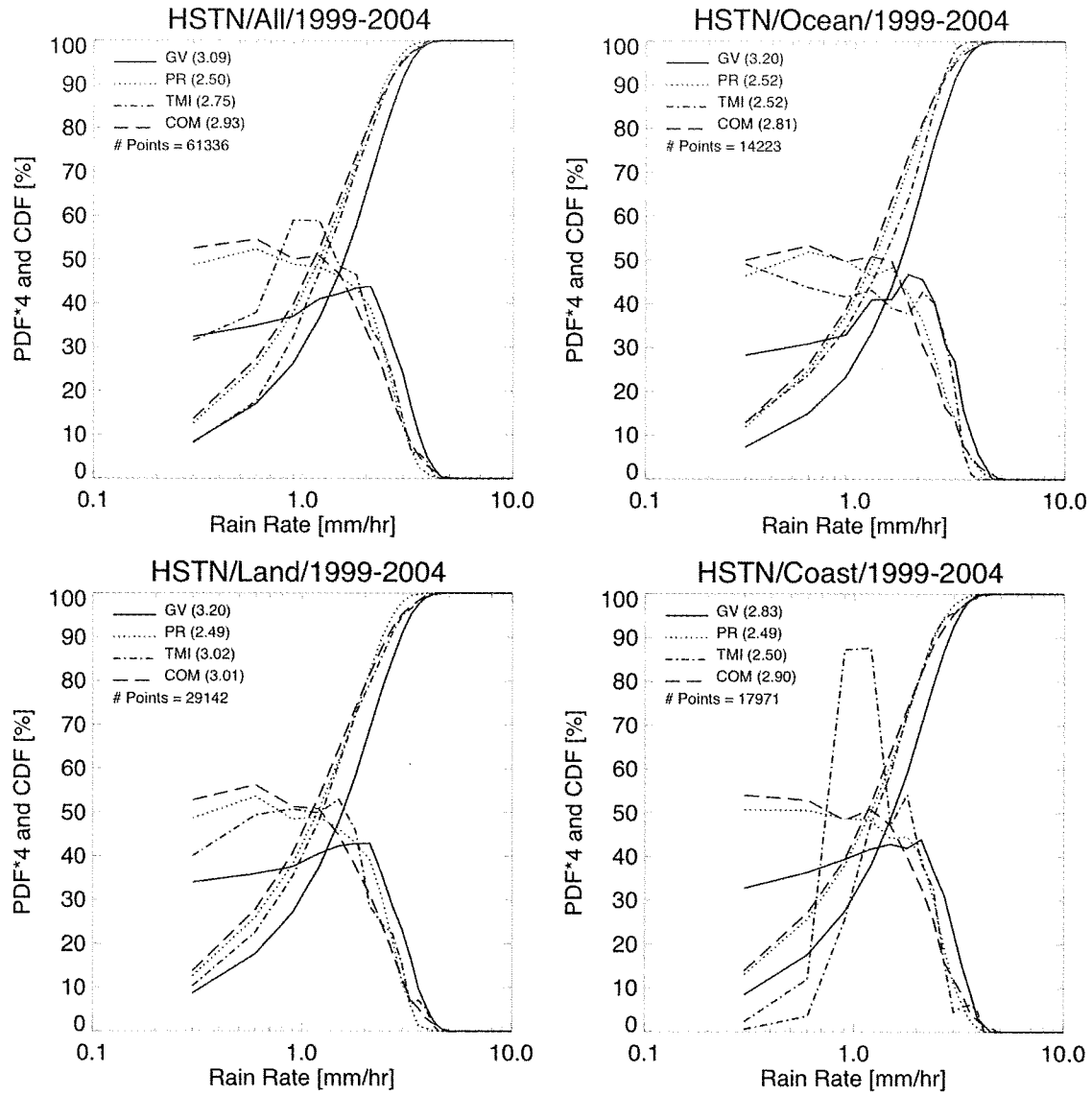


Fig. 18: Same as Fig. 18, except for HSTN.